Topological sensitivity-based analysis and optimization of microstructured interfaces

Marie Touboul, Rémi Cornaggia, Cédric Bellis

TOPOLOGICAL SENSITIVITY-BASED ANALYSIS AND OPTIMIZATION OF MICROSTRUCTURED INTERFACES*

MARIE TOUBOUL†, RÉMI CORNAGGIA ‡, AND CÉDRIC BELLIS §

Abstract. This paper concerns the optimization of microstructures when considering the propagation of scalar waves across a periodic row of inclusions embedded within a homogeneous matrix. The approach relies on the low-frequency homogenized model, which consists, in the present case, in some effective jump conditions. The topological derivatives of the effective parameters defining these jump conditions are computed from an asymptotic analysis. Their expressions are validated numerically and then used to study the sensitivity of the homogenized model to the geometry in case of elliptic inclusions. Finally, a topological optimization algorithm is used to minimize a given cost functional. This relies on the expression of the topological derivatives to iteratively perform phases changes in the unit cell characterizing the material, and on FFT-accelerated solvers previously adapted to solve the band cell problems underlying the homogenized model. To illustrate this approach, the resulting procedure is applied to the design of a microstructure that minimizes transmitted fields along a given direction.

Key words. topological optimization, asymptotic methods, periodic media, microstructured interface, effective jump conditions

1. Introduction.

The design of microstructured media allows to control wave propagation and may lead to exotic effects, e.g. negative refraction, subwavelength imaging, lensing and cloaking, to cite a few. It constitutes the paradigm of metamaterials, which have undergone spectacular developments since the early 2000: see [17] and references therein for an overview. An active direction of research concerns the size reduction of microstructures since it is often advantageous to replace a volumic distribution by a surfacic (in 3D) or a lineic (in 2D) distribution of scatterers, often called metasurface [8] or meta-interface.

The two-scale homogenization method is a privileged tool to approximate wave propagation in microstructured media [10, 37]. It avoids having to mesh fine spatial scales and gives an analytical insight on the macroscopic behaviour of waves. However, the usual homogenization methods fail when considering a thin row of scatterers, because of boundary effects at the transition between the scatterers and the homogenous medium in which it is embedded. To recover their efficiency, these methods must then be combined with matched-asymptotic expansions [24], yielding effective jump conditions on an equivalent meta-interface [19, 26, 18, 25, 36].

In the context of metamaterials, the optimization of the microstructures is a useful tool to determine designs that exhibit interesting macroscopic behaviours. To this purpose, different types of optimization can be considered: (i) the *parametric* optimization when the shapes are parameterised by a fixed number of variables (thickness, dimensions, etc.); (ii) the *shape* optimization when, from an initial shape, the position of the boundaries of the microstructure is changed without changing its topology; (iii) the *topological* optimization when the best possible geometry is sought, even if it means changing the topology. In this work, we are interested in topological optimization which leaves more freedom compared to the first two methods. The chosen

*Submitted to the editors DATE.

†Department of Mathematics, Imperial College London, Huxley Building, Queen's Gate, London SW7 2AZ, UK (m.touboul@imperial.ac.uk).

‡Sorbonne Université, CNRS, UMR 7190, Institut Jean Le Rond ∂'Alembert, F-75005 Paris, France (remi.cornaggia@sorbonne-universite.fr).

§Aix Marseille Univ, CNRS, Centrale Marseille, LMA, Marseille, France (bellis@lma.cnrs-mrs.fr).

mathematical tool to perform this type of optimization is the *topological derivative* [9] which measures the sensitivity of a cost functional to infinitesimal topological perturbations.

Then, different numerical methods can be employed to update the material properties based on the knowledge of the topological derivatives. One method used in this paper is the *level-set* method. For a two-phase material distribution, it relies on the characterization of this distribution thanks to a level-set function which is stricly positive in one phase and strictly negative in the other phase. This has first been introduced for *shape* optimization and is based on the fact that the interface between phases, which corresponds to the zero level-set function, can evolve based on the shape derivative of the cost functional with respect to a perturbation of this interface [1, 2]. This methodology has then been adapted to topological perturbation based on a projection algorithm [6, 7, 20, 33].

A strategy for microstructure optimization, in line with the homogenization considered in this paper, is to perform the optimization from the homogenized model that describes the material. It relies on the definition of a cost function, to be minimized, in terms of the effective coefficients that characterize the homogenized model. At low frequency, this method has been used in statics [7, 21, 33], in dynamics for a low constrast [2, 15], and a high contrast [40] of the physical properties (activating resonances of the highly contrasted inclusions). It has also been extended to optimize effective properties at high frequencies [32].

In this framework, a topological optimization procedure is presented in [15] to optimize dynamical properties for antiplane shear waves based on homogenization. The main ingredients are the following ones:

1. the two-scale asymptotic homogenization method is deployed,
2. a cost functional is constructed from the homogenized model,
3. its topological derivative is computed,
4. the cost functional minimization is performed thanks to a level-set algorithm,
5. the level-set is iterated by computed cell problems using FFT-accelerated solvers.

Noticeably, works on the optimization in dynamics of microstructured thin layers are more scarce and recent: [27] for an optimization of slabs based on far-field behaviour and [31] for a design of acoustic metasurfaces based on a homogenization model. In the present paper, we perform a sensitivity analysis and the optimization of an acoustic microstructured interface, based on the homogenized model of [25] and following the same overall approach than [15]. Novelties compared to [31] and [15] are (i) the derivation of topological derivatives and their use *prior to the topological optimization process* to perform a sensitivity analysis of the effective properties and to determine valuable initializations from the closed-form formula provided by the topological derivatives for elliptical inclusions; and (ii) the use of non-conventional FFT-based solvers to adress the specific *unbounded* cell problems that arise from the two-scale homogenization of microstructured interfaces.

The paper is organized as follows: the homogenized model is recalled in Section 2, and an analysis of smacroscopic observables is performed, so that a cost functional to minimize is proposed. In Section 3, the topological derivatives of the effective parameters of the interface model are derived and validated numerically. Then, in Section 4, based on the analytical information provided by these derivatives, a topological sensitivity-based analysis is performed for microstructures made of elliptic inclusions, and "asymptotically optimal" ellipses are determined for the chosen cost functional.

Then a topological optimization scheme which relies on the topological derivatives to update the material distribution at each iteration is presented in Section 5. We finally summarize the results and discuss possible perspectives in Section 6.

2. Microstructured interfaces and effective model.

2.1. Setting and homogenization. Let us consider the propagation of waves in two dimensions across a periodic row of inclusions $\cup_i \Omega_{\rm i}$ embedded within a homogeneous matrix Ω_m. The thickness and the period of the row are denoted by e and h, respectively, and we assume that $e = \mathcal{O}(h)$. The time and the spatial coordinates are denoted by t and $\boldsymbol{X} = (X_1, X_2)$, respectively, with X_2 being the direction of periodicity of the inclusions as shown in Figure 1. Anti-plane elastic waves are considered, and both media are assumed to be isotropic. The microstructured medium is therefore characterized by two constitutive parameters, the mass density ρ_h and the shear modulus μ_h, that are piecewise constant:

$$(\rho_h, \mu_h)(\boldsymbol{X}) = \begin{cases} (\rho_{\rm m}, \mu_{\rm m}) & \text{in the matrix,} \\ (\rho_{\rm i}, \mu_{\rm i}) & \text{in the inclusions,} \end{cases} \tag{2.1}$$

and the time-domain governing equation for the out-of-plane component U_h of the material displacement writes:

$$\boldsymbol{\nabla} \cdot \big(\mu_h(\boldsymbol{X}) \boldsymbol{\nabla} U_h(\boldsymbol{X}, t)\big) = \rho_h(\boldsymbol{X}) \frac{\partial^2 U_h}{\partial t^2}(\boldsymbol{X}, t). \tag{2.2}$$

Introducing the scalar velocity field $V_h = \partial U_h / \partial t$ and the stress vector $\boldsymbol{\Sigma}_h$ gathering the two shear components of the stress tensor, this system can be rewritten as a first-order system in time:

$$\begin{cases} \dfrac{\partial \boldsymbol{\Sigma}_h}{\partial t}(\boldsymbol{X}, t) = \mu_h(\boldsymbol{X}) \boldsymbol{\nabla} V_h(\boldsymbol{X}, t), \\ \rho_h(\boldsymbol{X}) \dfrac{\partial V_h}{\partial t}(\boldsymbol{X}, t) = \boldsymbol{\nabla} \cdot \boldsymbol{\Sigma}_h(\boldsymbol{X}, t), \end{cases} \tag{2.3}$$

with V_h and $\boldsymbol{\Sigma}_h \cdot \boldsymbol{n}$ being continuous at each matrix/inclusion interface $\partial\Omega_{\rm i}$, given that $\boldsymbol{n}$ is the *inward* unit normal on each $\partial\Omega_{\rm i}$.

Remark 2.1. The system (2.3) is also relevant to model other physical phenomena, such as acoustic waves for which the fields $\boldsymbol{\Sigma}_h$, V_h, ρ_h and $1/\mu_h$ would stand instead for in-plane particle velocity, acoustic pressure, compressibility and mass density, respectively.

The assumptions of the homogenization process and the results obtained in [25] are now briefly reminded.

Hypotheses of the homogenization process. Considering an illumination by an incident wave or external sources, a characteristic wavelength λ within the matrix is assumed to be much larger than the period h. Defining the wavenumber within the matrix as $k_m = 2\pi/\lambda$, we introduce the parameter

$$\eta = k_m h \tag{2.4}$$

and we assume that $\eta \ll 1$ for the configurations of interest.

Throughout this article, only the *non-resonant* case is adressed, i.e. the physical parameters of the matrix and of inclusions are supposed to be of the same order of

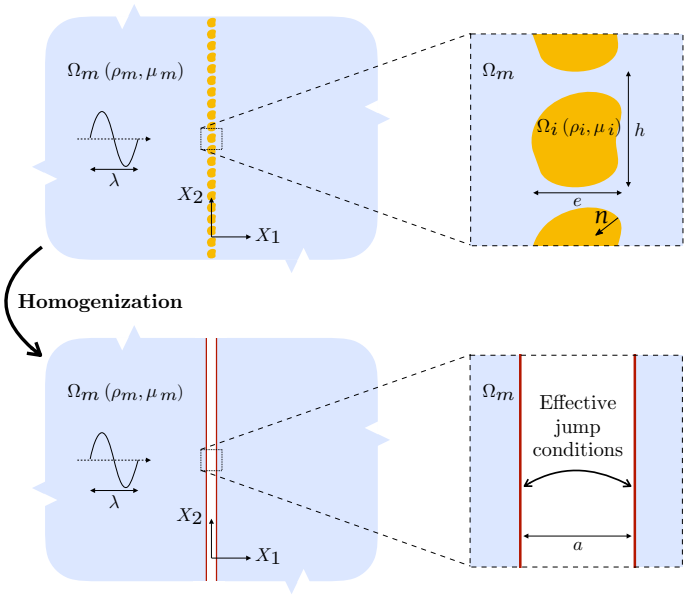

Fig. 1: Homogenization process for a single periodic array of inclusions. *(top)* Original configuration with a thin microstructured layer, *(bottom)* Homogenized interface model.

magnitude. For large contrasts, e.g. for very soft but dense inclusions ($\mu_\mathrm{i} \ll \mu_\mathrm{m}$ and $\rho_\mathrm{i} \sim \rho_\mathrm{m}$), the resonances of these inclusions play a key role in the transmission of waves, and should be captured by specific homogenization methods, see e.g. [36, 39] and the references therein.

These geometrical and material assumptions allows to homogenize the microstructure in the so-called long-wavelength, non-resonant regime.

Notations. The fast scale of coordinates is $\boldsymbol{y} = \boldsymbol{X}/h = (y_1, y_2)^\top$. The domain Ω is the elementary cell $\mathbb{R} \times [-1/2, 1/2]$ in $\boldsymbol{y}$-coordinates, see Figure 2, that is repeated periodically in the y_2 direction to obtain the full domain, and $(\boldsymbol{e}_1, \boldsymbol{e}_2)$ is the canonical basis of $\mathbb{R}^2$. For any function $f(x_1)$, we define the jump and the mean value around the (centered) enlarged interface of thickness a:

$$\llbracket f \rrbracket_a = f(a/2) - f(-a/2) \qquad \text{and} \qquad \langle f \rangle_a = \frac{1}{2}\big(f(a/2) + f(-a/2)\big). \tag{2.5}$$

We will also make use of the relative material constrasts τ^μ and tau^ρ defined by:

$$\tau^\mu = \frac{\mu_\mathrm{i} - \mu_\mathrm{m}}{\mu_\mathrm{m}} \quad \text{and} \quad \tau^\rho = \frac{\rho_\mathrm{i} - \rho_\mathrm{m}}{\rho_\mathrm{m}}. \tag{2.6}$$

Cell problems. The homogenization process requires the computation of auxiliary fields Φ_j for $j = 1, 2$ which are solutions of *elementary problems*. The problems initially proposed by [25] were posed on the semi-infinite representative cell Ω. For practical implementation the authors of the present paper proposed in [16] a refor-

mulation on a bounded rectangular cell Ω^a defined by:

$$\Omega^a = \left[-\frac{a}{2h}; \frac{a}{2h}\right] \times \underbrace{\left[-\frac{1}{2}; \frac{1}{2}\right]}_{I} \tag{2.7}$$

such that

$$\boldsymbol{m}(\boldsymbol{y}) := (\rho(\boldsymbol{y}), \mu(\boldsymbol{y})) = (\rho_{\mathrm{m}}, \mu_{\mathrm{m}}) \ \forall \boldsymbol{y} \in \Omega \backslash \Omega^a, \tag{2.8}$$

as represented in Figure 2. The parameter a used in the choice of the representative cell Ω^a also defines the *effective interface width*, see Figure 1. It should satisfy $a \geq e$ to ensure that the material variations are retrained to Ω^a, and for the effective model presented below to satisfy some stability conditions [25].

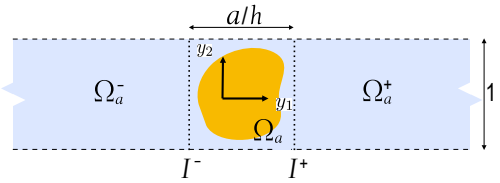

Fig. 2: Elementary cell Ω, decomposed into the bounded cell Ω^a, and half strips $\Omega_a^+ = [\frac{a}{2h}, +\infty[\times I$ and $\Omega_a^- =]-\infty, -\frac{a}{2h}] \times I$.

Using the notation $\boldsymbol{\Phi} = (\Phi_1, \Phi_2)$ for compactness, two (uncoupled) band cell problems are defined as:

$$\begin{cases} \boldsymbol{\nabla} \cdot (\mu(\boldsymbol{y}) (\boldsymbol{\nabla \Phi} + \boldsymbol{I}_2)) = \boldsymbol{0} \text{ in } \Omega^a, \\ \boldsymbol{\Phi} \text{ is } y_2\text{-periodic}, \\ \partial_n \boldsymbol{\Phi} \left(\pm \frac{a}{2h}, \cdot\right) = \boldsymbol{\Lambda} \left(\boldsymbol{\Phi} \left(\pm \frac{a}{2h}, \cdot\right)\right) \text{ on } I^{\pm}, \end{cases} \tag{2.9}$$

where $\boldsymbol{I}_2$ is the second-order identity tensor, (I^-, I^+) are the left and right boundaries of Ω^a (see Figure 2) and $\boldsymbol{\Lambda}$ is a nonlocal *Dirichlet-to-Neumann* (DtN) operator, whose expression is recalled in Appendix A for completeness. In (2.9) and hereafter, the adopted convention for the gradient components is such that $(\boldsymbol{\nabla \Phi})_{ij} = \partial \Phi_j / \partial y_i$.

These elementary solutions will serve to compute the effective parameters that appear in the homogenized model presented now.

Homogenized model. From [25], we know that the homogenization of the problem (2.3) at order $\mathcal{O}(\eta)$ in such a configuration yields the following homogenized model:

$$\begin{cases} \dfrac{\partial \boldsymbol{\Sigma}}{\partial t} = \mu_{\mathrm{m}} \boldsymbol{\nabla} V & (|X_1| \geq a/2,\ X_2 \in \mathbb{R}), \\ \rho_{\mathrm{m}} \dfrac{\partial V}{\partial t} = \boldsymbol{\nabla} \cdot \boldsymbol{\Sigma} & (|X_1| \geq a/2,\ X_2 \in \mathbb{R}), \\ [\![V]\!]_a = h \left\{ \mathcal{B} \left\langle \dfrac{\partial V}{\partial X_1} \right\rangle_a + \mathcal{B}_2 \left\langle \dfrac{\partial V}{\partial X_2} \right\rangle_a \right\} & (X_2 \in \mathbb{R}), \\ [\![\Sigma_1]\!]_a = h \left\{ \mathcal{S} \left\langle \boldsymbol{\nabla} \cdot \boldsymbol{\Sigma} \right\rangle_a - \mathcal{C}_1 \left\langle \dfrac{\partial \Sigma_1}{\partial X_2} \right\rangle_a - \mathcal{C} \left\langle \dfrac{\partial \Sigma_2}{\partial X_2} \right\rangle_a \right\} & (X_2 \in \mathbb{R}), \end{cases} \tag{2.10}$$

featuring imperfect transmission conditions for the velocity V and normal component of the stress vector Σ_1. The *effective coefficients* entering these conditions are the parameter

$$\mathcal{S} = \frac{a}{h} + \tau^{\rho}|\Omega_{\mathrm{i}}| \tag{2.11}$$

where $|\Omega_{\mathrm{i}}| = \int_{\Omega_{\mathrm{i}}} \mathrm{d}\boldsymbol{y}$ is the surface of the inclusion phase in the rescaled coordinates; and the four coefficients $(\mathcal{B}, \mathcal{B}_2, \mathcal{C}_1, \mathcal{C})$ gathered in the two vector-valued parameters $\boldsymbol{\mathcal{B}} = (\mathcal{B}, \mathcal{B}_2)$ and $\boldsymbol{\mathcal{C}} = (\mathcal{C}_1, \mathcal{C})$, which are expressed in terms of the elementary solution $\boldsymbol{\Phi}$ to (2.9) as:

$$\boldsymbol{\mathcal{B}}(\boldsymbol{m}) = \frac{a}{h}\boldsymbol{e}_1 + \int_I \left[\boldsymbol{\Phi}\left(\frac{a}{2h}, y_2\right) - \boldsymbol{\Phi}\left(-\frac{a}{2h}, y_2\right)\right] \mathrm{d}y_2, \tag{2.12}$$

and:

$$\boldsymbol{\mathcal{C}}(\boldsymbol{m}) = \int_{\Omega^a} \frac{\mu(\boldsymbol{y})}{\mu_{\mathrm{m}}} \left(\frac{\partial \boldsymbol{\Phi}}{\partial y_2}(\boldsymbol{y}) + \boldsymbol{e}_2\right) \mathrm{d}\boldsymbol{y}. \tag{2.13}$$

The effective parameters characterizing the homogenized medium are finally collected in $\boldsymbol{m}_{\mathrm{eff}}$ as:

$$\boldsymbol{m}_{\mathrm{eff}} = (\mathcal{B}, \mathcal{B}_2, \mathcal{S}, \mathcal{C}_1, \mathcal{C}), \tag{2.14}$$

with the relation $\mathcal{B}_2 = -\mathcal{C}_1$ that has been proven in [25].

2.2. Analysis of macroscopic observables. When the frequency-domain formulation of (2.10) and an incident plane wave is considered, the expression of the associated reflexion and transmission coefficients of the interface can be obtained analytically [38]. For an incident plane wave at angle θ_{I} with the horizontal axis, these coefficients read respectively:

$$\begin{cases} \mathcal{R}(\theta_{\mathrm{I}}, \omega) = \dfrac{\mathrm{i}\omega\,\mathscr{L}}{\mathscr{Z} + \mathrm{i}\omega\,\mathscr{N} - \omega^2\mathscr{M}} \exp\left(\mathrm{i}\dfrac{\omega}{c_m} a\cos\theta_{\mathrm{I}}\right), \\ \mathcal{T}(\theta_{\mathrm{I}}, \omega) = \dfrac{\mathscr{Z} + \mathrm{i}\omega\,\mathscr{G} + \omega^2\mathscr{M}}{\mathscr{Z} + \mathrm{i}\omega\,\mathscr{N} - \omega^2\mathscr{M}} \exp\left(\mathrm{i}\dfrac{\omega}{c_m} a\cos\theta_{\mathrm{I}}\right), \end{cases} \tag{2.15}$$

with $c_m = \sqrt{\mu_m/\rho_m}$ and

$$\begin{cases} \mathscr{L} = h\left(\mathcal{B}\cos(\theta_{\mathrm{I}})^2 + \mathcal{C}\sin(\theta_{\mathrm{I}})^2 - \mathcal{S}\right), \\ \mathscr{Z} = 2c_m\cos\theta_{\mathrm{I}}, \\ \mathscr{N} = h\left(-\mathcal{C}\sin(\theta_{\mathrm{I}})^2 + \mathcal{B}\cos(\theta_{\mathrm{I}})^2 + \mathcal{S}\right), \\ \mathscr{M} = \dfrac{h^2}{2c_m}\left(\mathcal{B}_2\mathcal{C}_1\sin(\theta_{\mathrm{I}})^2 - \mathcal{B}\mathcal{C}\sin(\theta_{\mathrm{I}})^2 + \mathcal{B}\mathcal{S}\right)\cos(\theta_{\mathrm{I}}), \\ \mathscr{G} = -h(-\mathcal{C}_1 + \mathcal{B}_2)\cos(\theta_{\mathrm{I}})\sin(\theta_{\mathrm{I}}). \end{cases} \tag{2.16}$$

One can notice a symmetry with respect to the normal incidence $\theta_I = 0$ for the reflexion coefficient $\mathcal{R}(\theta_{\mathrm{I}}, \omega)$ and for the modulus of the transmission coefficient $|\mathcal{T}(\theta_{\mathrm{I}}, \omega)|$. Consequently, only the argument of the transmission coefficient $\arg(\mathcal{T}(\theta_{\mathrm{I}}, \omega))$ is not symmetric with respect to the normal incidence. The quantity $\mathscr{G}$ defined in (2.16) and proportional to $\mathcal{B}_2 = -\mathcal{C}_1$ is responsible for this asymmetry. Therefore, one can

Table 1: Physical parameters considered for the microstructure.

$\mu_{\rm i}$	$\rho_{\rm i}$	$\mu_{\rm m}$	$\rho_{\rm m}$
78 GPa	$7800\text{kg}\cdot\text{m}^{-3}$	12 GPa	$2500\text{kg}\cdot\text{m}^{-3}$

wonder if a directional macroscopic effect can be obtained for geometries associated with non-null values of this effective parameter, which corresponds to cases when the microstructure is not symmetric with respect to the X_2-axis [25].

To investigate qualitatively this question, one considers a microstructure typical of steel in concrete, for which physical parameters are given by Table 1. The periodicity length is $h = 1$m and the examples of two geometries for the inclusion $\Omega_{\rm i}$ are investigated: one ellipse of semi-axes lengths (0.15, 0.5) tilted of $-\pi/4$ and one rectangle of sizes (1.25, 0.08) tilted of $-\pi/4$. The effective parameters associated to these two configurations are computed and time-domain simulations are performed in the associated effective media for $\boldsymbol{X} \in [-70;35] \times [-132;132]$. The excitation is a source $\delta(\boldsymbol{X} - \boldsymbol{X}_{\rm S})g(t)$ with $g(t)$ defined as:

$$g(t) = \begin{cases} A \displaystyle\sum_{m=1}^{4} a_m \, \sin(\beta_m \, \omega_c \, t) & \text{if } 0 < t < \dfrac{1}{f_c}, \\ 0 \ \text{otherwise}, \end{cases} \tag{2.17}$$

where $\beta_m = 2^{m-1}$ and the coefficients a_m being $a_1 = 1$, $a_2 = -21/32$, $a_3 = 63/768$, $a_4 = -1/512$. It entails that $g \in C^6([0,+\infty[)$ and $g(t)$ is a wide-band signal with a central frequency $f_c = \omega_c/2\pi$. The source is located at $\boldsymbol{X}_{\rm S} = (-35, 0)$, with $X_1 = 0$ being the center of the enlarged effective interface. The central frequency is $f_c = 50$ Hz which corresponds to a small parameter $\eta = 0.14$ for which a good agreement between the homogenized model and the microstructured configuration has been observed. The time-domain simulations are performed thanks to Finite Differences and to the Explicit Simplified Interface Method [23] to handle the effective enlarged interface.

The scattered fields are computed from time $t = 0$ until $t_{\rm f} = 86.7$ ms. From these data, one can compute the cumulative energy defined as:

$$\mathcal{E}(\boldsymbol{X}) = \frac{1}{2}\int_0^{t_{\rm f}} \left(\frac{1}{\mu_{\rm m}} \boldsymbol{\Sigma}(\boldsymbol{X},t)^2 + \rho_{\rm m} V(\boldsymbol{X},t)^2 \right) {\rm d}t. \tag{2.18}$$

This quantity is displayed for both microstructures in Figures 3a and 3b as a function of the polar coordinates (r, θ) centered at $\boldsymbol{X}_{\rm S}$, with $r \in [40;60]$, passed the interface. The red crosses denote for a given value of r, the value of the critical angle $\theta_{\rm C}$ for which $\mathcal{E}$ is minimal. One can notice that this value $\theta_{\rm C}$ seems to be independant of r. Furthermore, the sign of $\arg(\mathcal{T})$ is plotted in Figures 3c and 3d for the same two microstructures directly using the analytical formula (2.16), as a function of θ_I and ω. It is then observed that this critical value measured on time-domain simulations (denoted by the blue cross) seems to coincide with a change of sign in $\arg(\mathcal{T})$ at low frequency.

To have an analytical insight into this critical value $\theta_{\rm C}$ at low frequency, one considers a first-order approximation for $\mathcal{T}$. Upon introducing $\bar{\mathscr{G}} = \mathscr{G}/h$, $\bar{\mathscr{M}} = 2c_m\mathscr{M}/h^2$ and

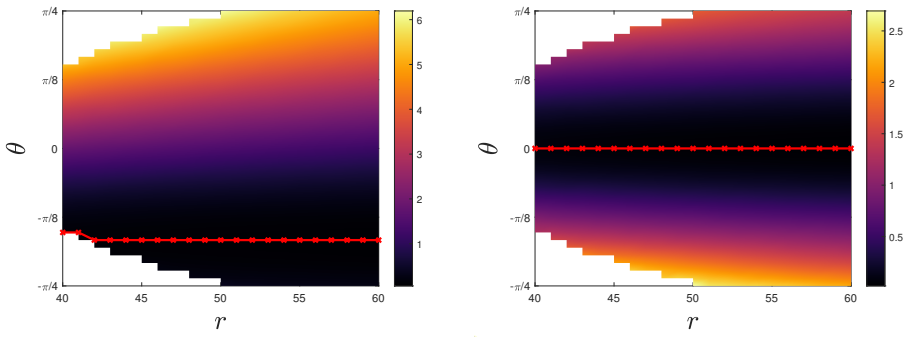

(a) $\mathcal{E}(r,\theta)$ for elliptic inclusions

(b) $\mathcal{E}(r,\theta)$ for rectangular inclusions

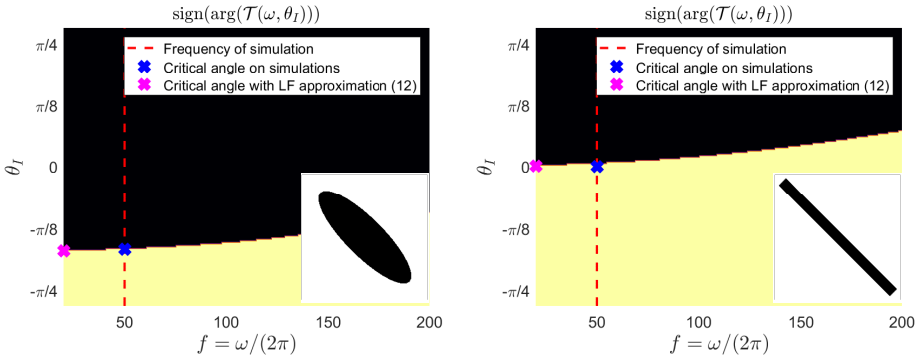

(c) sign(arg($\mathcal{T}$)) for elliptic inclusions

(d) sign(arg($\mathcal{T}$)) for rectangular inclusions

Fig. 3: Cumulative energy (first row) where the position of the minimal value for a given r is denoted by the red crosses, and study of sign(arg($\mathcal{T}$)) (second row, yellow and black for positive and negative signs, respectively), computed with the effective model corresponding to elliptic (left) and rectangular (right) inclusions.

$\bar{\mathcal{N}} = \mathcal{N}/h$, this leads to:

$$
\begin{aligned}
\mathcal{T}(\theta_{\mathrm{I}},\omega) &= \frac{\mathscr{L} + \mathrm{i}\eta c_m \bar{\mathscr{G}} + \eta^2 \frac{c_m}{2}\bar{\mathscr{M}}}{\mathscr{L} + \mathrm{i}\eta c_m \bar{\mathcal{N}} - \eta^2 \frac{c_m}{2}\bar{\mathscr{M}}} \exp\left(\mathrm{i}\eta \frac{a}{h}\cos(\theta_{\mathrm{I}})\right) \\
&= \frac{1 + \mathrm{i}\eta \frac{\bar{\mathscr{G}}}{2\cos(\theta_{\mathrm{I}})} + \mathcal{O}(\eta^2)}{1 + \mathrm{i}\eta \frac{\bar{\mathcal{N}}}{2\cos(\theta_{\mathrm{I}})} + \mathcal{O}(\eta^2)} (1 + \mathrm{i}\eta \frac{a}{h}\cos(\theta_{\mathrm{I}}) + \mathcal{O}(\eta^2)) \\
&= 1 + \mathrm{i}\eta \left(\frac{\bar{\mathscr{G}} - \bar{\mathcal{N}}}{2\cos(\theta_{\mathrm{I}})} + \frac{a}{h}\cos(\theta_{\mathrm{I}}) \right) + \mathcal{O}(\eta^2).
\end{aligned}
\tag{2.19}
$$

This can be summarized as

$$
\mathcal{T}(\theta_{\mathrm{I}},\omega) = 1 + \mathrm{i}\eta\, \mathcal{T}_1(\boldsymbol{m}_{\mathrm{eff}},\theta_{\mathrm{I}}) + \mathcal{O}(\eta^2) \tag{2.20}
$$

with $\mathcal{T}_1(\boldsymbol{m}_{\text{eff}}, \theta_{\text{I}})$ given by

$$\begin{aligned}\mathcal{T}_1(\boldsymbol{m}_{\text{eff}}, \theta_{\text{I}}) &= -\mathcal{B}_2 \sin(\theta_{\text{I}}) + \frac{\mathcal{C}\sin(\theta_{\text{I}})^2 - \mathcal{B}\cos(\theta_{\text{I}})^2 - \mathcal{S}}{2\cos(\theta_{\text{I}})} + \frac{a}{h}\cos(\theta_{\text{I}}) \\ &= -\mathcal{B}_2 \sin(\theta_{\text{I}}) + \frac{\mathcal{C}^\star \sin(\theta_{\text{I}})^2 - \mathcal{B}^\star \cos(\theta_{\text{I}})^2 - \mathcal{S}^\star}{2\cos\theta_{\text{I}}},\end{aligned} \tag{2.21}$$

where

$$\mathcal{B}^\star = \mathcal{B} - a/h, \quad \mathcal{C}^\star = \mathcal{C} - a/h, \quad \text{and} \quad \mathcal{S}^\star = \mathcal{S} - a/h = \tau^\rho |\Omega_{\text{i}}|. \tag{2.22}$$

The second expression in (2.21), using the coefficients in (2.22) shows that $\mathcal{T}_1$ does not depend on the choice of interface thickness a and will be used in Section 4 to slightly simplify the computations.

With this approximation (2.20), it is clear that, at low frequency, $\arg(\mathcal{T})$ changes sign when $\mathcal{T}_1(\boldsymbol{m}_{\text{eff}}, \theta_{\text{I}})$ changes sign. This is confirmed in Figures 3c and 3d (black and yellow maps where yellow and black stand for positive and negative sign, respectively) where the angle for which $\mathcal{T}_1$ changes sign is denoted by a pink cross and is observed to be very close to both the critical angle observed in numerical simulations and the angle for which the exact value of $\arg(\mathcal{T})$ changes sign at low frequency.

This function $\mathcal{T}_1$ then seems to be an interesting quantity to study and control in order to get a desired macroscopic directive effect, i.e. a cumulative energy which is minimal at a given angle $\theta_{\min}$. Therefore, the following functional to minimize is introduced

$$\mathcal{J}_{\text{main}}(\boldsymbol{m}_{\text{eff}}) = \left(\frac{\mathcal{T}_1(\boldsymbol{m}_{\text{eff}}, \theta_{\min})}{\partial_\theta \mathcal{T}_1(\boldsymbol{m}_{\text{eff}}, \theta_{\min})} \right)^2, \quad \text{with: } \partial_\theta \mathcal{T}_1 = \frac{\partial \mathcal{T}_1}{\partial \theta_{\text{I}}}, \tag{2.23}$$

where we aim at simultaneously maximizing the derivative amplitude $|\partial_\theta \mathcal{T}_1|$ to (i) avoid close-to-zero local minima of $|\mathcal{T}_1|$ without sign change and (ii) "push" the ensuing optimization process towards "stiff" sign changes.

There are mainly two objectives in this paper: (i) the computation of the topological sensitivity of the effective parameters $\boldsymbol{m}_{\text{eff}}$ to changes of the microstructures and (ii) the generation of a phase distribution $\boldsymbol{m}_{\text{opt}}$ in the bounded cell Ω^a that optimizes an objective cost functional $\mathcal{J}(\boldsymbol{m}_{\text{eff}})$ such as (2.23).

Regarding the second objective, additional terms will be added to the functional $\mathcal{J}_{\text{main}}$ in (2.23) in order to reach a given surface ratio between the materials, or to have a sufficient smoothness of the final configuration. This will be discussed through the introduction of a total cost functional $\mathcal{J}$ and an optimization process in Section 5.3. The topological derivatives derived in Section 3, and the optimization methods described in Section 5.1 could however be used for any other objective.

3. Topological derivatives of the effective parameters. In this section, one aims at describing the sensitivity of the effective parameters to periodic topological changes of the microstructure, i.e. geometric perturbations of the representative cell Ω^a. A perturbation is defined as a small inhomogeneity $\mathcal{P}_{\boldsymbol{z},\varepsilon} = \boldsymbol{z} + \varepsilon\mathcal{P}$ of size ε, normalized shape $\mathcal{P}$ and physical parameters $(\mu + \Delta\mu, \rho + \Delta\rho)$ introduced at a point $\boldsymbol{z} \in \Omega^a$. The material perturbation is $\Delta\boldsymbol{m} = (\Delta\rho, \Delta\mu)$ with $\Delta\mu > -\min_{\boldsymbol{y}\in\Omega^a} \mu(\boldsymbol{y})$ and $\Delta\rho > -\min_{\boldsymbol{y}\in\Omega^a} \rho(\boldsymbol{y})$ to satisfy the physical constraints. The resulting perturbed cell, denoted by $\Omega^a_{\boldsymbol{z},\varepsilon}$ and represented in Figure 4, features the physical parameters

$$\boldsymbol{m}_{\boldsymbol{z},\varepsilon} = (\mu_{\boldsymbol{z},\varepsilon}, \rho_{\boldsymbol{z},\varepsilon}) = (\mu + \Delta\mu \chi_{\mathcal{P}_{\boldsymbol{z},\varepsilon}}, \rho + \Delta\rho \chi_{\mathcal{P}_{\boldsymbol{z},\varepsilon}}), \tag{3.1}$$

with $\chi_{\mathcal{P}_{\boldsymbol{z},\varepsilon}}$ the characteristic function of the perturbation domain $\mathcal{P}_{\boldsymbol{z},\varepsilon}$. The definition of $\Delta\boldsymbol{m}$ may depend on the choice of $\boldsymbol{z}$ if the unperturbed cell is heterogeneous. However, we disregard the case where the perturbation is located at an interface between two different materials. Consequently, we will drop any dependence of $\Delta\boldsymbol{m}$ on the space coordinate in the notations, since they don't change the integrals computed hereafter.

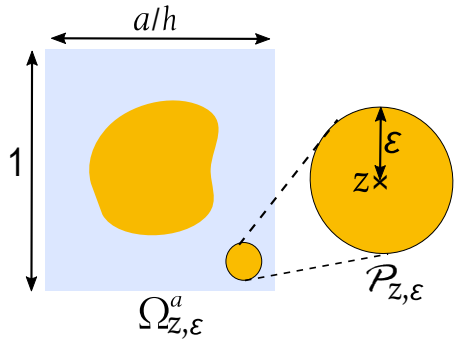

Fig. 4: Cell $\Omega^a_{\boldsymbol{z},\varepsilon}$ perturbed by the introduction of the inhomogeneity $\mathcal{P}_{\boldsymbol{z},\varepsilon}$.

Let f be a function of the material properties. In this two-dimensional context, the so-called *topological derivative* of a given function f, denoted by $\mathcal{D}f$, is defined thanks to the following 2D asymptotic expansion:

$$f_{\boldsymbol{z},\varepsilon} \coloneqq f(\boldsymbol{m}_{\boldsymbol{z},\varepsilon}) \underset{\varepsilon\to 0}{=} f(\boldsymbol{m}) + \varepsilon^2 \mathcal{D}f(\boldsymbol{m},\boldsymbol{z},\mathcal{P},\Delta\boldsymbol{m}) + o(\varepsilon^2). \tag{3.2}$$

It describes the influence on the functional f of a perturbation located at $\boldsymbol{z}$, of shape $\mathcal{P}$ and material perturbation $\Delta\boldsymbol{m}$. Therefore, the more negative $\mathcal{D}f(\boldsymbol{m},\boldsymbol{z},\mathcal{P},\Delta\boldsymbol{m})$ is, the more efficient such a perturbation at point $\boldsymbol{z}$ would be to decrease f.

In this section, the topological derivatives of the effective parameters collected in (2.14) are computed. First, one looks for an expansion solution $\boldsymbol{\Phi}_{\boldsymbol{z},\varepsilon}$ to the cell problem (2.9) in the perturbed cell Ω^a_ε in Section 3.1. This allows the computation of the topological sensitivities of the five effective parameters in Section 3.2.

3.1. Approximation of the perturbed cell problem solution. To compute the topological derivatives of the homogenized coefficients, we must characterize the asymptotic behavior of the cell function $\boldsymbol{\Phi}$ in (2.9) when the perturbation is introduced. To this end, we first reformulate the cell problem (2.9) into an integral equation, more suitable for the asymptotic analysis. This formulation will be used formally to compute the topological derivatives, but we do not claim it is an equivalent variational formulation of it.

Weak forms of the unperturbed and perturbed cell problems. The first step is to write the weak form of the cell problem. To do so, we consider a function $v \in H^1_{\text{per}} = \left\{u \in H^1(\Omega^a;\mathbb{R}),\ u\ y_2\text{-periodic}\right\}$. The first equation of (2.9) is then multiplied by v and integrated by parts in Ω^a. Using the periodic condition and the boundary condition in (2.9), one obtains after a division by μ_{m}:

$$\boldsymbol{\mathcal{A}}_\mu(\boldsymbol{\Phi},v) = -\boldsymbol{F}_\mu(v) + \boldsymbol{J}(v) \qquad \forall v \in H^1_{\text{per}} \tag{3.3}$$

where one has introduced the following functionals for $\boldsymbol{u} = (u_1, u_2) \in H^1_{\mathrm{per}} \times H^1_{\mathrm{per}}$ and $v \in H^1_{\mathrm{per}}$:

$$\begin{cases} \boldsymbol{\mathcal{A}}_\mu(\boldsymbol{u}, v) = \displaystyle\int_{\Omega^a} \frac{\mu(\boldsymbol{y})}{\mu_{\mathrm{m}}} \boldsymbol{\nabla} \boldsymbol{u}(\boldsymbol{y})^\top \cdot \boldsymbol{\nabla} v(\boldsymbol{y}) \mathrm{d}\boldsymbol{y} + \mathcal{L}^-(\boldsymbol{u}, v) + \mathcal{L}^+(\boldsymbol{u}, v), \\ \boldsymbol{F}_\mu(v) = \displaystyle\int_{\Omega^a} \frac{\mu(\boldsymbol{y})}{\mu_{\mathrm{m}}} \boldsymbol{\nabla} v(\boldsymbol{y}) \mathrm{d}\boldsymbol{y}, \\ \boldsymbol{J}(v) = \displaystyle\int_I \left[v\left(\frac{a}{2h}, y_2\right) - v\left(-\frac{a}{2h}, y_2\right) \right] \boldsymbol{e}_1 \mathrm{d}y_2, \end{cases} \tag{3.4}$$

with

$$\mathcal{L}^{\pm}(\boldsymbol{u}, v) = -\int_I \boldsymbol{\Lambda}\left[\boldsymbol{u}\left(\pm\frac{a}{2h}, \cdot\right)\right](y_2)\, v\left(\pm\frac{a}{2h}, y_2\right) \mathrm{d}y_2. \tag{3.5}$$

This vector-valued weak-formulation is a short-hand notation for the two uncoupled equations satisfied by $\boldsymbol{\Phi} = (\Phi^{(1)}, \Phi^{(2)})$.

Similarly, the perturbed field $\boldsymbol{\Phi}_{\boldsymbol{z},\varepsilon}$ satisfies for all $v \in H^1(\Omega^a; \mathbb{R})$, v y_2-periodic:

$$\boldsymbol{\mathcal{A}}_{\mu_{\boldsymbol{z},\varepsilon}}(\boldsymbol{\Phi}_{\boldsymbol{z},\varepsilon}, v) = -\boldsymbol{F}_\mu(v) - \boldsymbol{\delta F}_{\boldsymbol{z},\varepsilon}(v) + \boldsymbol{J}(v), \tag{3.6}$$

with

$$\boldsymbol{\delta F}_{\boldsymbol{z},\varepsilon}(v) = \frac{\Delta\mu}{\mu_{\mathrm{m}}} \int_{\mathcal{P}_{\boldsymbol{z},\varepsilon}} \boldsymbol{\nabla} v(\boldsymbol{y}) \mathrm{d}\boldsymbol{y}. \tag{3.7}$$

Integral equation. To obtain the integral equation satisfied by $\boldsymbol{\Phi}_{\boldsymbol{z},\varepsilon}$, one then introduces the Green's function $G(\cdot, \boldsymbol{x})$ associated with a point source at $\boldsymbol{x} \in \Omega^a$, i.e. the solution of

$$\begin{cases} -\boldsymbol{\nabla}_{\boldsymbol{y}} \cdot \left(\dfrac{\mu(\boldsymbol{y})}{\mu_{\mathrm{m}}} \boldsymbol{\nabla}_{\boldsymbol{y}} G(\boldsymbol{y}, \boldsymbol{x}) \right) = \delta(\boldsymbol{y} - \boldsymbol{x}) \quad \forall \boldsymbol{y} \in \Omega^a, \\ G(\cdot, \boldsymbol{x}) \ y_2\text{-periodic}, \\ -\boldsymbol{n} \cdot \boldsymbol{\nabla}_{\boldsymbol{y}} G(\boldsymbol{y}, \boldsymbol{x}) \Big|_{y_1 = \pm\frac{a}{2h}} = \boldsymbol{\Lambda}\left[G(\boldsymbol{y}, \boldsymbol{x})\right] \Big|_{y_1 = \pm\frac{a}{2h}} \quad \forall \boldsymbol{y} \in I^{\pm}. \end{cases} \tag{3.8}$$

It can be decomposed as

$$G(\boldsymbol{y}, \boldsymbol{x}) = G_\infty\left(\boldsymbol{y} - \boldsymbol{x}; \frac{\mu(\boldsymbol{x})}{\mu_{\mathrm{m}}}\right) + G_c(\boldsymbol{y}, \boldsymbol{x}), \quad \text{with} \quad G_\infty(\boldsymbol{r}; \mu_\star) = -\frac{\ln(\|\boldsymbol{r}\|)}{2\pi\mu_\star}, \tag{3.9}$$

where G_∞ is the full-space Green's function solution of 2D Poisson equation that shares the same singularity as G, and G_c is the complementary part to the Green's function solution accounting for the heterogeneity of the cell and the boundary conditions. Detail on these functions is given in Appendix B.

For any sufficiently smooth function $\boldsymbol{w}$, one gets from (3.8) the integral representation for all $\boldsymbol{x} \in \Omega^a$:

$$\boldsymbol{w}(\boldsymbol{x}) = \boldsymbol{\mathcal{A}}_\mu(\boldsymbol{w}, G(\cdot, \boldsymbol{x})) \tag{3.10}$$

with $\boldsymbol{\mathcal{A}}_\mu$ defined in (3.4).

Coming back to the perturbed problem, one introduces the surface integral operator $\boldsymbol{\mathcal{N}}_{\boldsymbol{z},\varepsilon}$:

$$\boldsymbol{\mathcal{N}}_{\boldsymbol{z},\varepsilon}\boldsymbol{f}(\boldsymbol{x}) = \frac{\Delta\mu}{\mu_{\mathrm{m}}}\int_{\mathcal{P}_{\boldsymbol{z},\varepsilon}} \boldsymbol{\nabla}\boldsymbol{f}(\boldsymbol{y})^{\top}\cdot\boldsymbol{\nabla}_{\boldsymbol{y}}G(\boldsymbol{y},\boldsymbol{x})\mathrm{d}\boldsymbol{y}. \tag{3.11}$$

Taking $v = G(\cdot,\boldsymbol{x})$ in (3.6) together with the definition (3.4) of $\boldsymbol{\mathcal{A}}_{\mu}$ then yields

$$\begin{aligned}\boldsymbol{\mathcal{A}}_{\mu}(\boldsymbol{\Phi}_{\boldsymbol{z},\varepsilon},G(\cdot,\boldsymbol{x})) + \boldsymbol{\mathcal{N}}_{\boldsymbol{z},\varepsilon}\boldsymbol{\Phi}_{\boldsymbol{z},\varepsilon}(\boldsymbol{x}) &= -\boldsymbol{F}_{\mu}(G(\cdot,\boldsymbol{x})) - \boldsymbol{\delta}\boldsymbol{F}_{\boldsymbol{z},\varepsilon}(G(\cdot,\boldsymbol{x})) + \boldsymbol{J}(G(\cdot,\boldsymbol{x}))\\ &= \boldsymbol{\mathcal{A}}_{\mu}(\boldsymbol{\Phi},G(\cdot,\boldsymbol{x})) - \boldsymbol{\delta}\boldsymbol{F}_{\boldsymbol{z},\varepsilon}(G(\cdot,\boldsymbol{x})),\end{aligned} \tag{3.12}$$

where in the last line we used $v = G(\cdot,\boldsymbol{x})$ in (3.3). Finally, one considers $\boldsymbol{w} = \boldsymbol{\Phi}_{\boldsymbol{z},\varepsilon}$ and $\boldsymbol{w} = \boldsymbol{\Phi}$ in (3.10). Together with (3.12) this leads to the integral equation satisfied by the perturbed field $\boldsymbol{\Phi}_{\boldsymbol{z},\varepsilon}$:

$$(\boldsymbol{I} + \boldsymbol{\mathcal{N}}_{\boldsymbol{z},\varepsilon})(\boldsymbol{\Phi}_{\boldsymbol{z},\varepsilon})(\boldsymbol{x}) = \boldsymbol{\Phi}(\boldsymbol{x}) - \boldsymbol{\delta}\boldsymbol{F}_{\boldsymbol{z},\varepsilon}(G(\cdot,\boldsymbol{x})), \tag{3.13}$$

where the integral operator $\boldsymbol{\mathcal{N}}_{\boldsymbol{z},\varepsilon}$ and right-hand side term $\boldsymbol{\delta}\boldsymbol{F}_{\boldsymbol{z},\varepsilon}(G(\cdot,\boldsymbol{x}))$ are both supported by the perturbation domain $\mathcal{P}_{\boldsymbol{z},\varepsilon}$.

Asymptotic analysis. Aiming at reformulating the equation (3.13) onto the reference shape $\mathcal{P}$, let us introduce the scaled coordinates $\boldsymbol{x} = \boldsymbol{z} + \varepsilon\bar{\boldsymbol{x}}$ and assume the following expansion for all $\boldsymbol{x} \in \mathcal{P}_{\boldsymbol{z},\varepsilon}$:

$$\boldsymbol{\Phi}_{\boldsymbol{z},\varepsilon}(\boldsymbol{x}) = \boldsymbol{\Phi}(\boldsymbol{z}) + \varepsilon\boldsymbol{\Phi}_1(\bar{\boldsymbol{x}}) + o(\varepsilon). \tag{3.14}$$

One also writes the following Taylor expansion for the cell function

$$\boldsymbol{\Phi}(\boldsymbol{x}) = \boldsymbol{\Phi}(\boldsymbol{z}) + \varepsilon\bar{\boldsymbol{x}}\cdot\boldsymbol{\nabla}\boldsymbol{\Phi}(\boldsymbol{z}) + o(\varepsilon). \tag{3.15}$$

Inserting (3.14) and (3.15) in (3.13) and keeping only the leading and first-order terms yields, since $\boldsymbol{\mathcal{N}}_{\boldsymbol{z},\varepsilon}\boldsymbol{\Phi}(\boldsymbol{z}) = \boldsymbol{0}$:

$$(\boldsymbol{I} + \boldsymbol{\mathcal{N}}_{\boldsymbol{z},\varepsilon})\left(\varepsilon\boldsymbol{\Phi}_1\left(\frac{\cdot - \boldsymbol{z}}{\varepsilon}\right)\right)(\boldsymbol{x}) = \varepsilon\bar{\boldsymbol{x}}\cdot\boldsymbol{\nabla}\boldsymbol{\Phi}(\boldsymbol{z}) - \boldsymbol{\delta}\boldsymbol{F}_{\boldsymbol{z},\varepsilon}(G(\cdot,\boldsymbol{x})). \tag{3.16}$$

As developed in Appendix B, $\boldsymbol{\nabla}G_{\infty}$ is homogeneous of degree -1 (see (B.1)) and $\boldsymbol{\nabla}G_c(\cdot,\boldsymbol{x})$ is regular in the neighborhood of $\boldsymbol{z}$ (see (B.4)). The function G in (3.8) then satisfies:

$$\boldsymbol{\nabla}_{\boldsymbol{y}}G(\boldsymbol{y},\boldsymbol{x}) = \varepsilon^{-1}\boldsymbol{\nabla}G_{\infty}\left(\bar{\boldsymbol{y}} - \bar{\boldsymbol{x}}; \frac{\mu(\boldsymbol{z})}{\mu_{\mathrm{m}}}\right) + o(\varepsilon^{-1}). \tag{3.17}$$

Inserting the above expansion in (3.16), performing a change of variable to rewrite the integral on $\mathcal{P}$ and identifying the leading-order ($O(\varepsilon)$) contributions then leads to the scaled integral equation:

$$(\boldsymbol{I} + \boldsymbol{\mathcal{M}})(\widetilde{\boldsymbol{\Phi}}_1)(\bar{\boldsymbol{x}}) = \bar{\boldsymbol{x}}\cdot(\boldsymbol{\nabla}\boldsymbol{\Phi}(\boldsymbol{z}) + \boldsymbol{I}), \tag{3.18}$$

with $\widetilde{\boldsymbol{\Phi}}_1(\bar{\boldsymbol{x}}) = \boldsymbol{\Phi}_1(\bar{\boldsymbol{x}}) + \bar{\boldsymbol{x}}$ and $\boldsymbol{\mathcal{M}}$ defined by

$$\boldsymbol{\mathcal{M}}\boldsymbol{f}(\bar{\boldsymbol{x}}) = \frac{\Delta\mu}{\mu_{\mathrm{m}}}\int_{\mathcal{P}} \boldsymbol{\nabla}\boldsymbol{f}(\bar{\boldsymbol{y}})^{\top}\cdot\boldsymbol{\nabla}G_{\infty}\left(\bar{\boldsymbol{y}} - \bar{\boldsymbol{x}}; \frac{\mu(\boldsymbol{z})}{\mu_{\mathrm{m}}}\right)\mathrm{d}\bar{\boldsymbol{y}}. \tag{3.19}$$

Consequently, introducing $\boldsymbol{R}$, the vector solution of the equation:

$$(\boldsymbol{I}+\boldsymbol{\mathcal{M}})\boldsymbol{R}(\bar{\boldsymbol{x}})=\bar{\boldsymbol{x}} \tag{3.20}$$

i.e. the solution to a free-space transmission problem associated with a perturbation $(\mathcal{P},\Delta\mu)$, with an homogeneous background of modulus $\mu(\boldsymbol{z})$, then $\widetilde{\boldsymbol{\Phi}}_1$ is given by:

$$\widetilde{\boldsymbol{\Phi}}_1(\bar{\boldsymbol{x}})=\boldsymbol{R}(\bar{\boldsymbol{x}})\cdot(\boldsymbol{\nabla}\boldsymbol{\Phi}(\boldsymbol{z})+\boldsymbol{I}). \tag{3.21}$$

Finally, one inserts this in (3.14) to get the first-order expansion:

$$\boldsymbol{\Phi}_{\boldsymbol{z},\varepsilon}(\boldsymbol{x})=\boldsymbol{\Phi}(\boldsymbol{z})+\varepsilon\left(\boldsymbol{R}(\bar{\boldsymbol{x}})\cdot(\boldsymbol{\nabla}\boldsymbol{\Phi}(\boldsymbol{z})+\boldsymbol{I})-\bar{\boldsymbol{x}}\right)+o(\varepsilon). \tag{3.22}$$

3.2. Calculation of the topological derivatives. The results of this section are summarized in the following proposition:

Proposition 3.1. The topological derivatives of the effective coefficients $\mathcal{S},\boldsymbol{\mathcal{B}},\boldsymbol{\mathcal{C}}$, for a material perturbation $(\Delta\mu,\Delta\rho)$ supported by the domain $\mathcal{P}_{\boldsymbol{z},\varepsilon}=\boldsymbol{z}+\varepsilon\mathcal{P}$, are given by :

$$\mathcal{DS}(\boldsymbol{m},\boldsymbol{z},\mathcal{P},\Delta\boldsymbol{m})=\frac{\Delta\rho}{\rho_{\mathrm{m}}}|\mathcal{P}|, \tag{3.23}$$

$$\boldsymbol{\mathcal{DB}}(\boldsymbol{m},\boldsymbol{z},\mathcal{P},\Delta\boldsymbol{m})=-(\boldsymbol{\nabla}\Phi_1(\boldsymbol{z})+\boldsymbol{e}_1)\cdot\boldsymbol{A}(\mathcal{P},\mu(\boldsymbol{z}),\Delta\mu)\cdot(\boldsymbol{\nabla}\boldsymbol{\Phi}(\boldsymbol{z})+\boldsymbol{I}), \tag{3.24}$$

$$\boldsymbol{\mathcal{DC}}(\boldsymbol{m},\boldsymbol{z},\mathcal{P},\Delta\boldsymbol{m})=(\boldsymbol{\nabla}\Phi_2(\boldsymbol{z})+\boldsymbol{e}_2)\cdot\boldsymbol{A}(\mathcal{P},\mu(\boldsymbol{z}),\Delta\mu)\cdot(\boldsymbol{\nabla}\boldsymbol{\Phi}(\boldsymbol{z})+\boldsymbol{I}), \tag{3.25}$$

where the so-called polarization second-order tensor $\boldsymbol{A}$ is defined from the solution $\boldsymbol{R}$ of the problem (3.20) as

$$\boldsymbol{A}(\mathcal{P},\mu(\boldsymbol{z}),\Delta\mu)=\frac{\Delta\mu}{\mu_{\mathrm{m}}}\int_{\mathcal{P}}\boldsymbol{\nabla}_{\bar{\boldsymbol{y}}}\boldsymbol{R}(\bar{\boldsymbol{y}})\mathrm{d}\bar{\boldsymbol{y}}. \tag{3.26}$$

Remark 3.2. The polarization tensor $\boldsymbol{A}$ (also called concentration or localization tensor [34]) has been used in previous studies [14, 3, 12]. It is symmetric and is known analytically for a variety of inclusion shapes $\mathcal{P}$, see [34]. In particular, for an elliptic perturbation of semiaxes lengths (1,γ) along directions $(\boldsymbol{a}_1,\boldsymbol{a}_2)$, it is given by:

$$\boldsymbol{A}(\mathcal{P},\mu(\boldsymbol{z}),\Delta\mu)=\pi\gamma(\gamma+1)\frac{\Delta\mu}{\mu_{\mathrm{m}}}\left(\frac{\boldsymbol{a}_1\otimes\boldsymbol{a}_1}{1+\gamma+\gamma\frac{\Delta\mu}{\mu(\boldsymbol{z})}}+\frac{\boldsymbol{a}_2\otimes\boldsymbol{a}_2}{1+\gamma+\frac{\Delta\mu}{\mu(\boldsymbol{z})}}\right). \tag{3.27}$$

The steps leading to the expressions above are now given.

3.2.1. Computation of $\mathcal{DS}$. We first notice that, owing to the definition of $\mathcal{S}$ in (2.11), one has

$$\mathcal{S}(\boldsymbol{m})=\int_{\Omega^a}\frac{\rho(\boldsymbol{y})}{\rho_{\mathrm{m}}}\mathrm{d}\boldsymbol{y}. \tag{3.28}$$

Consequently, one gets

$$\mathcal{S}_{\boldsymbol{z},\varepsilon}=\quad\mathcal{S}(\boldsymbol{m})+\int_{\mathcal{P}_{\boldsymbol{z},\varepsilon}}\frac{\Delta\rho}{\rho_{\mathrm{m}}}\mathrm{d}\boldsymbol{y}=\mathcal{S}(\boldsymbol{m})+\varepsilon^2\frac{\Delta\rho}{\rho_{\mathrm{m}}}|\mathcal{P}| \tag{3.29}$$

which yields by identification with (3.2) the following result

$$\mathcal{DS}(\boldsymbol{m},\boldsymbol{z},\mathcal{P},\Delta\boldsymbol{m})=\frac{\Delta\rho}{\rho_{\mathrm{m}}}|\mathcal{P}|. \tag{3.30}$$

3.2.2. Computation of $\mathcal{DB}$. From the expression (2.12), the effective parameter $\boldsymbol{\mathcal{B}}_{\boldsymbol{z},\varepsilon}$ associated with the perturbed cell writes

$$\boldsymbol{\mathcal{B}}_{\boldsymbol{z},\varepsilon} = \boldsymbol{\mathcal{B}}(\boldsymbol{m}) + \int_I \left[\boldsymbol{\delta\Phi}_{\boldsymbol{z},\varepsilon}\left(\frac{a}{2h}, y_2\right) - \boldsymbol{\delta\Phi}_{\boldsymbol{z},\varepsilon}\left(-\frac{a}{2h}, y_2\right)\right] \mathrm{d}y_2, \tag{3.31}$$

with the pertubation for the solution of the cell problem $\boldsymbol{\delta\Phi}_{\boldsymbol{z},\varepsilon}$ defined by

$$\boldsymbol{\delta\Phi}_{\boldsymbol{z},\varepsilon} = \boldsymbol{\Phi}_{\boldsymbol{z},\varepsilon} - \boldsymbol{\Phi}. \tag{3.32}$$

The left-hand side of (3.6) writes

$$\boldsymbol{\mathcal{A}}_{\mu_{\boldsymbol{z},\varepsilon}}(\boldsymbol{\Phi}_{\boldsymbol{z},\varepsilon}, v) = \boldsymbol{\mathcal{A}}_{\mu}(\boldsymbol{\Phi}, v) + \boldsymbol{\mathcal{A}}_{\mu}(\boldsymbol{\delta\Phi}_{\boldsymbol{z},\varepsilon}, v) + \frac{\Delta\mu}{\mu_{\mathrm{m}}} \int_{\mathcal{P}_{\boldsymbol{z},\varepsilon}} \boldsymbol{\nabla\Phi}_{\boldsymbol{z},\boldsymbol{\varepsilon}}(\boldsymbol{y})^{\top} \cdot \boldsymbol{\nabla} v(\boldsymbol{y}) \mathrm{d}\boldsymbol{y}. \tag{3.33}$$

Inserting this equation in (3.6) and using (3.3), one gets for all $v \in H^1_{\mathrm{per}}$:

$$\boldsymbol{\mathcal{A}}_{\mu}(\boldsymbol{\delta\Phi}_{\boldsymbol{z},\varepsilon}, v) + \frac{\Delta\mu}{\mu_{\mathrm{m}}} \int_{\mathcal{P}_{\boldsymbol{z},\varepsilon}} \boldsymbol{\nabla\Phi}_{\boldsymbol{z},\boldsymbol{\varepsilon}}(\boldsymbol{y})^{\top} \cdot \boldsymbol{\nabla} v(\boldsymbol{y}) \mathrm{d}\boldsymbol{y} = -\boldsymbol{\delta F}_{\boldsymbol{z},\varepsilon}(v). \tag{3.34}$$

Furthermore, $\beta = \Phi^{(1)} + y_1$ satisfies for all $\boldsymbol{w} \in H^1(\Omega^a; \mathbb{R}^2)$, $\boldsymbol{w}$ y_2-periodic

$$\boldsymbol{\mathcal{A}}_{\mu}(\boldsymbol{w}, \beta) = \int_I \left[\boldsymbol{w}\left(\frac{a}{2h}, y_2\right) - \boldsymbol{w}\left(-\frac{a}{2h}, y_2\right)\right] \mathrm{d}y_2. \tag{3.35}$$

Taking $v = \beta$ in (3.34) and $\boldsymbol{w} = \boldsymbol{\delta\Phi}_{\boldsymbol{z},\varepsilon}$ in (3.35), the expansion (3.31) writes

$$\boldsymbol{\mathcal{B}}_{\boldsymbol{z},\varepsilon} = \boldsymbol{\mathcal{B}}(\boldsymbol{m}) - \frac{\Delta\mu}{\mu_{\mathrm{m}}} \int_{\mathcal{P}_{\boldsymbol{z},\varepsilon}} \boldsymbol{\nabla}\beta(\boldsymbol{y}) \cdot (\boldsymbol{\nabla\Phi}_{\boldsymbol{z},\varepsilon}(\boldsymbol{y}) + \boldsymbol{I}) \mathrm{d}\boldsymbol{y}. \tag{3.36}$$

Consequently, one looks for an asymptotic expansion for $\boldsymbol{\nabla\Phi}_{\boldsymbol{z},\varepsilon}$. For this purpose, one uses the final expansion (3.22) of the previous section. One also writes the expansion $\boldsymbol{\nabla}\beta(\boldsymbol{y}) = \boldsymbol{\nabla}\beta(\boldsymbol{z}) + o(1)$ for all $\boldsymbol{y} \in \mathcal{P}_{\boldsymbol{z},\varepsilon}$ and expresses the integral in the scaled coordinates as

$$\boldsymbol{\mathcal{B}}_{\boldsymbol{z},\varepsilon} = \boldsymbol{\mathcal{B}}(\boldsymbol{m}) - \frac{\Delta\mu}{\mu_{\mathrm{m}}} \int_{\mathcal{P}} \boldsymbol{\nabla}\beta(\boldsymbol{z}) \cdot \left(\frac{1}{\varepsilon}\boldsymbol{\nabla\Phi}_{\boldsymbol{z},\varepsilon}(\bar{\boldsymbol{y}}) + \boldsymbol{I}\right) \varepsilon^2 \mathrm{d}\bar{\boldsymbol{y}} + o(\varepsilon^2). \tag{3.37}$$

Inserting the expansion (3.22) in the above equation yields

$$\boldsymbol{\mathcal{B}}_{\boldsymbol{z},\varepsilon} = \boldsymbol{\mathcal{B}}(\boldsymbol{m}) - \varepsilon^2 \frac{\Delta\mu}{\mu_{\mathrm{m}}} \boldsymbol{\nabla}\beta(\boldsymbol{z}) \cdot \int_{\mathcal{P}} \boldsymbol{\nabla R}(\bar{\boldsymbol{y}}) \mathrm{d}\bar{\boldsymbol{y}} \cdot (\boldsymbol{\nabla\Phi}(\boldsymbol{z}) + \boldsymbol{I}) + o(\varepsilon^2). \tag{3.38}$$

Using the definition the definition $\beta = \Phi_1 + y_1$ and the polarization tensor $\boldsymbol{A}$ defined by (3.26), the topological derivative of $\boldsymbol{\mathcal{B}}$ writes

$$\boldsymbol{\mathcal{DB}}(\boldsymbol{m}, \boldsymbol{z}, \mathcal{P}, \Delta\boldsymbol{m}) = -(\boldsymbol{\nabla}\Phi_1(\boldsymbol{z}) + \boldsymbol{e}_1) \cdot \boldsymbol{A}(\mathcal{P}, \mu(\boldsymbol{z}), \Delta\mu) \cdot (\boldsymbol{\nabla\Phi}(\boldsymbol{z}) + \boldsymbol{I}). \tag{3.39}$$

3.2.3. Computation of $\mathcal{DC}$. From the expression (2.13), the effective parameter $\boldsymbol{\mathcal{C}}_{\boldsymbol{z},\varepsilon}$ associated with the perturbed cell writes

$$\boldsymbol{\mathcal{C}}_{\boldsymbol{z},\varepsilon} = \boldsymbol{\mathcal{C}}(\boldsymbol{m}) + \int_{\Omega^a} \frac{\mu(\boldsymbol{y})}{\mu_{\mathrm{m}}} \frac{\partial \boldsymbol{\delta\Phi}_{\boldsymbol{z},\varepsilon}}{\partial y_2}(\boldsymbol{y}) \mathrm{d}\boldsymbol{y} + \frac{\Delta\mu}{\mu_{\mathrm{m}}} \int_{\mathcal{P}_{\boldsymbol{z},\varepsilon}} \left(\frac{\partial \boldsymbol{\Phi}_{\boldsymbol{z},\varepsilon}}{\partial y_2}(\boldsymbol{y}) + \boldsymbol{e}_2\right) \mathrm{d}\boldsymbol{y} + o(\varepsilon^2). \tag{3.40}$$

We know that Φ_2 satisfies for all $\boldsymbol{w} \in H^1_{\text{per}}$

$$\boldsymbol{\mathcal{A}}_\mu(\boldsymbol{w}, \Phi_2) = -\int_{\Omega^a} \frac{\mu(\boldsymbol{y})}{\mu_{\text{m}}} \frac{\partial \boldsymbol{w}}{\partial y_2}(\boldsymbol{y}) \mathrm{d}\boldsymbol{y}. \tag{3.41}$$

One takes $v = \Phi_2$ in (3.34) and $\boldsymbol{w} = \boldsymbol{\delta\Phi}_{\boldsymbol{z},\varepsilon}$ in (3.41) and gets

$$\int_{\Omega^a} \frac{\mu(\boldsymbol{y})}{\mu_{\text{m}}} \frac{\partial \boldsymbol{\delta\Phi}_{\boldsymbol{z},\varepsilon}}{\partial y_2}(\boldsymbol{y}) \mathrm{d}\boldsymbol{y} = \frac{\Delta\mu}{\mu_{\text{m}}} \int_{\mathcal{P}_{\boldsymbol{z},\varepsilon}} \boldsymbol{\nabla}\Phi_2(\boldsymbol{y}) \cdot (\boldsymbol{\nabla\Phi}_{\boldsymbol{z},\varepsilon}(\boldsymbol{y}) + \boldsymbol{I}) \mathrm{d}\boldsymbol{y}, \tag{3.42}$$

which yields

$$\boldsymbol{\mathcal{C}}_{\boldsymbol{z},\varepsilon} = \boldsymbol{\mathcal{C}}(\boldsymbol{m}) + \frac{\Delta\mu}{\mu_{\text{m}}} \int_{\mathcal{P}_{\boldsymbol{z},\varepsilon}} (\boldsymbol{\nabla}\Phi_2(\boldsymbol{y}) + \boldsymbol{e}_2) \cdot (\boldsymbol{\nabla\Phi}_{\boldsymbol{z},\varepsilon}(\boldsymbol{y}) + \boldsymbol{I}) \mathrm{d}\boldsymbol{y} + o(\varepsilon^2). \tag{3.43}$$

Once again, we use the Taylor expansion $\boldsymbol{\nabla}\Phi_2(\boldsymbol{y}) = \boldsymbol{\nabla}\Phi_2(\boldsymbol{z}) + o(1)$ for all $\boldsymbol{y}$ in $\mathcal{P}_{\boldsymbol{z},\varepsilon}$, the expression of the integral in the scaled coordinates and the expansion (3.22) to get the final expression for the topological derivative

$$\boldsymbol{\mathcal{DC}}(\boldsymbol{m}, \boldsymbol{z}, \mathcal{P}, \Delta\boldsymbol{m}) = (\boldsymbol{\nabla}\Phi_2(\boldsymbol{z}) + \boldsymbol{e}_2) \cdot \boldsymbol{A}(\mathcal{P}, \mu(\boldsymbol{z}), \Delta\mu) \cdot (\boldsymbol{\nabla\Phi}(\boldsymbol{z}) + \boldsymbol{I}). \tag{3.44}$$

3.3. Numerical validation. To validate numerically the found expressions of the topological derivatives, we can compute the error made by the approximation of $\boldsymbol{\mathcal{B}}_{\boldsymbol{z},\varepsilon}$ and $\boldsymbol{\mathcal{C}}_{\boldsymbol{z},\varepsilon}$ by $\boldsymbol{\mathcal{B}} + \varepsilon^2\boldsymbol{\mathcal{DB}}$ and $\boldsymbol{\mathcal{C}} + \varepsilon^2\boldsymbol{\mathcal{DC}}$, respectively. Indeed, due to (3.38) and (3.43), this error should be of order ε^3 at least.

One starts with an initial reference configuration ($\varepsilon = 0$), computes numerically the solutions of the cell problems (2.9) (their computation will be briefly described in Section 5.1.1), and thus the value of $\boldsymbol{\mathcal{B}}$ and $\boldsymbol{\mathcal{C}}$ from (2.12) and (2.13). The initial configuration is chosen to be heterogenous in order to avoid simplifications than can occur with a homogeneous medium as reference. More precisely, we choose a homogenous medium containing an ellipsoidal inclusion of center $(0, 0)$ and semixes lengths $(0.32\,\text{m},\ 0.1\,\text{m})$, tilted of 45°. The physical parameters are again given by Table 1. Then one inserts a perturbation in the background matrix at $\boldsymbol{z} = (-0.26\ \text{m}, 0.24\ \text{m})$.

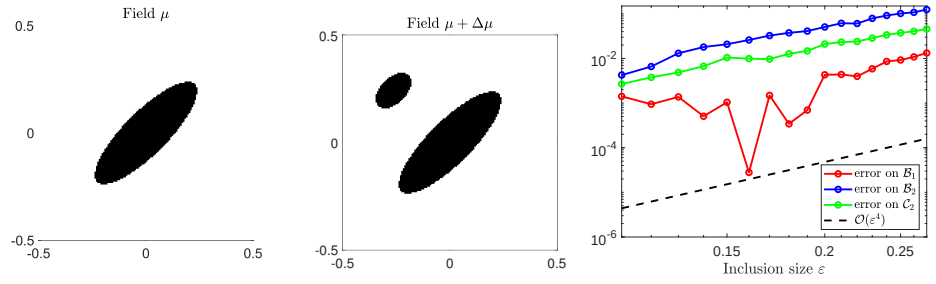

(a) Reference Ω^a (b) Perturbed cell $\Omega^a_{\boldsymbol{z},\varepsilon}$ (c)

Fig. 5: Test case for an ellipsoidal perturbation: (a) Reference configuration (b) Perturbed onfiguration for $\varepsilon = 0.1$. (c) Relative error between the exact and approximated effectives parameters as a function of ε in a log-log scale.

Its physical parameters are the ones of the ellipsoidal inclusion $(\rho_\mathrm{i}, \mu_\mathrm{i})$. Its shape is an ellipse of semiaxes lengths $(\varepsilon, 0.6\,\varepsilon)$ and tilted of 45°. For $\varepsilon = 0.1$, the configuration is plotted in Figure 5b. For a given value of ε, one computes the perturbed cell solutions and thus the exact effective parameters $\boldsymbol{\mathcal{B}}_{\boldsymbol{z},\varepsilon}$ and $\boldsymbol{\mathcal{C}}_{\boldsymbol{z},\varepsilon}$ from (2.12) and (2.13). Their first-order approximations $\boldsymbol{\mathcal{B}} + \varepsilon^2\boldsymbol{\mathcal{D}\mathcal{B}}$ and $\boldsymbol{\mathcal{C}} + \varepsilon^2\boldsymbol{\mathcal{D}\mathcal{C}}$ are computed from (3.24) and (3.25) using (3.27).

The relative errors (e.g. $|(\mathcal{B}^\star)_{\boldsymbol{z},\varepsilon} - \mathcal{B}^\star - \varepsilon^2\mathcal{D}\mathcal{B}_1|/|(\mathcal{B}^\star)_{\boldsymbol{z},\varepsilon}|$) between both the exact and approximated values are plotted as functions of perturbation size ε in log-log scale in Figure 5c. Since $\mathcal{B}_2 = \mathcal{C}_1$, only one of the corresponding misfit is represented. The dashed line stands for an error of $\mathcal{O}(\varepsilon^4)$. It seems that this is the actual order of approximation of the effective parameters, the small variations for low values of ε being probably due to numerical errors in the computation of the coefficients. This underlines the fact that the leading order term and consequently the topological derivatives are well accounted for and that the terms of order ε^3 in the expansions (3.38) and (3.43) are probably equal to zero for this type of perturbations with a central symmetry. This was already observed for the volumic case in [11, 12], with the intuition that it occurs for perturbations with a central symmetry. This remains however to be proved.

4. Topological sensitivity-based analysis of the effective parameters for elliptic inclusions.

In this section, the topological derivatives are used as tools to analyse the case of cells made of a unique *elliptic* inclusion Ω_i in a homogenous material. First, the quality of the approximation of the effective parameters in this case is investigated. Then, we show that "asymptotically optimal" elliptic shapes can be determined for our choice of cost functional, i.e. shapes for which the leading-order contribution to the cost functionnal, given by the topological derivative, vanishes.

4.1. Approximation of the effective parameters.

Consider a unique inclusion in an otherwise homogeneous cell, a configuration which can be seen as a single perturbation in a homogeneous reference cell. In this case, the effective coefficient $\mathcal{S}^\star = \mathcal{S} - a/h$ in (2.22) is given by the exact expression:

$$\mathcal{S}^\star = \varepsilon^2|\mathcal{P}|\tau^\rho, \tag{4.1}$$

where the topological derivatives formula provide the following approximations:

$$\mathcal{B}^\star = -\varepsilon^2 A_{11} + o(\varepsilon^2), \quad \mathcal{B}_2 = -\varepsilon^2 A_{12} + o(\varepsilon^2), \quad \mathcal{C}^\star = \varepsilon^2 A_{22} + o(\varepsilon^2). \tag{4.2}$$

Computing these approximations only requires the knowledge of the polarization tensor (3.27) for the perturbation shape $\mathcal{P}$, and the scaling of the result by ε^2. This is much less costly than computing numerically the cell solutions and the associated effective parameters for each choice of inclusion, especially for elliptic inclusions for which the polarization tensor is known analytically.

As an example of the quality of these approximations, we consider an ellipse, located at $\boldsymbol{z} = (0, 0)$, of tilted angle 40°, and semiaxes lengths $(\varepsilon, 0.2\,\varepsilon)$. In Figure 6b, the relative errors between the numerically computed value of the effective parameters through (2.12-2.13) and their approximations given above are represented for an increasing value of ε. We first note that the order of convergence of the *relative* error is of $\mathcal{O}(\varepsilon^2)$ in this case because the zeroth-order term in the denominator vanishes when the reference configuration is homogeneous. We also observe that a good agreement is obtained even for high values of ε (i.e. even outisde of the asymptotic regime).

Indeed, for $\varepsilon = 0.5$ (illustrated in Figure 6a) the major axis length is equal to the size of the unit cell and the relative errors remain below 15%.

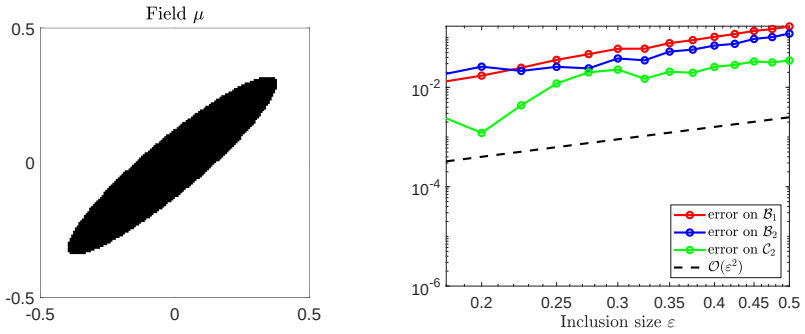

(a) (b)

Fig. 6: Test case for an ellipsoidal inclusion: (a) Configuration for $\varepsilon = 0.5$. (b) Relative errors between the exact and approximated effectives parameters as functions of inclusion size ε in a log-log scale.

Remark 4.1. The approximation (4.2), using only the polarization tensor computed from the free-space transmission problem (3.20), is well-known in the domain of micromechanics as the "dilute" or "Eshelby" approximation (see for instance [34] and the numerous references therein). It does not account for interactions between inclusions, and is therefore supposedly restricted to very low concentrations of inclusions, but provides surprisingly accurate results in the present context.

Consequently, we propose to use the expressions (4.2) to obtain "optimal" ellipses that minimize the chosen functional (2.23).

4.2. Normal incidence: explicit formula and analysis. When the case of interest is normal incidence of waves, i.e. when $\theta_{\mathrm{I}} = 0$, closed-form results are available, that are used in this section as a first example of minimization of a cost functional finding an optimal ellipse. Indeed, the expression (2.20) of the function of interest $\mathcal{T}_1$ is considerably simplified:

$$\mathcal{T}_1(\theta_{\mathrm{I}} = 0) = -\frac{1}{2}\left(\mathcal{B}^\star + \mathcal{S}^\star\right) = -\frac{\varepsilon^2}{2}\left(-A_{11} + \pi\gamma\tau^\rho\right) + o(\varepsilon^2). \tag{4.3}$$

Then, couples (θ, γ) for which $\mathcal{T}_1 = o(\varepsilon^2)$ can be found analytically for given material contrasts (τ^ρ, τ^μ). Indeed, canceling the leading-order term above and introducing the expression (3.27) of the polarization tensor gives:

$$\pi\gamma\tau^\rho = A_{11} \Leftrightarrow \quad \tau^\rho = (1+\gamma)\tau^\mu\left(\frac{\cos^2(\theta)}{1+\gamma+\gamma\tau^\mu} + \frac{\sin^2(\theta)}{1+\gamma+\tau^\mu}\right) \tag{4.4}$$

which leads to

$$\tau^\rho(1+\gamma+\gamma\tau^\mu)(1+\gamma+\tau^\mu) - \tau^\mu(1+\gamma)^2 - (\tau^\mu)^2(1+\gamma)(\gamma+(1-\gamma)\cos^2(\theta)) = 0. \tag{4.5}$$

Therefore, we eventually get

(4.6)
$$\begin{cases} \theta = \arccos\sqrt{\beta} & \text{if } \beta \geq 0 \\ \text{no solution} & \text{if } \beta < 0 \end{cases}, \quad \text{with } \beta = \frac{\left[\tau^\rho(1+\gamma+\tau^\mu) - \tau^\mu(1+\gamma)\right](1+\gamma+\gamma\tau^\mu)}{(\tau^\mu)^2(1-\gamma^2)}.$$

This particular solution can be used used to check the numerical implementation of $\mathcal{T}_1$.

To find an optimal couple $(\theta^{\text{opt}}, \gamma^{\text{opt}})$ with respect to the cost functionnal (2.23) we furthermore look for the maximal absolute value of the derivative, $|\partial_\theta \mathcal{T}_1(\theta_{\text{I}} = 0)|$, along the curve defined by the function (4.6) above. To do so, we rely again on the simplified expression of the function $\partial_\theta \mathcal{T}_1$ for normal incidence ($\theta_{\text{I}} = 0$) and on the approximations (4.2) of the effective coefficients, and use the approximation:

(4.7)
$$\begin{aligned} \partial_\theta \mathcal{T}_1(\theta_{\text{I}} = 0) = -\mathcal{B}_2 &= \varepsilon^2 A_{12} + o(\varepsilon^2) \\ &= \frac{\varepsilon^2 \sin(2\theta)}{2} \frac{\pi\gamma(1-\gamma^2)(\tau^\mu)^2}{[1+\gamma(1+\tau^\mu)][1+\gamma+\tau^\mu]} + o(\varepsilon^2). \end{aligned}$$

Then plugging the expression (4.6) of θ, one obtains an expression for the leading-order contribution of $\partial_\theta \mathcal{T}_1$ as a function of γ only, whose maximum is easily found numerically, as represented in Figure 7.

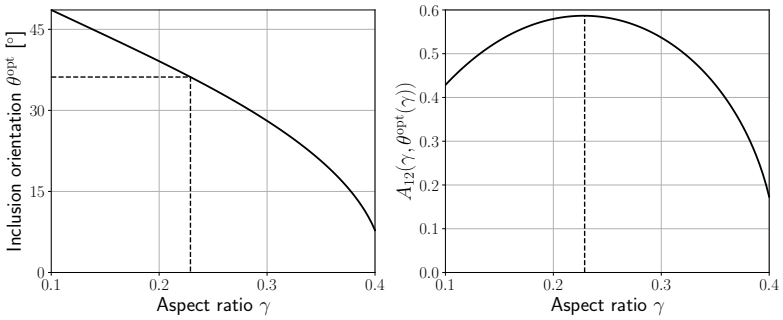

Fig. 7: Left: Curve $\theta(\gamma)$ corresponding to $\mathcal{T}_1(\theta_{\text{I}} = 0) = o(\varepsilon^2)$. Right: coefficient A_{12}, i.e. leading-order contribution of $\partial_\theta \mathcal{T}_1(\theta_{\text{I}} = 0)$, along this curve. Positions of the optimal parameters $(\theta^{\text{opt}}, \gamma^{\text{opt}})$ are given in dashed lines.

Finally, the numerical "true" values of the homogenized coefficients and functions $\mathcal{T}_1$, $\partial_\theta \mathcal{T}_1$ and $\mathcal{J}_{\text{main}}$ are computed for non-vanishing inclusions, of increasing finite size ε, as plotted in Figure 8. As expected, the value of $\mathcal{T}_1$ and therefore the cost functional $\mathcal{J}_{\text{main}}$ (2.23) diverge from their asymptotic values. Nevertheless, as summarized in Table 2, the ellipse parametrized by $(\theta^{\text{opt}}, \gamma^{\text{opt}})$ gives significantly better results (lower values of $\mathcal{T}_1$ and $\mathcal{J}_{\text{main}}$) than a disk or an arbitrarily chosen ellipse with equal surface ratio, also represented in Figure 8.

This asymptotic analysis therefore provides good "first guess" that can be used as initial guess for toplogical optimization procedures as seen in the next section.

4.3. Arbitrary incidence: numerical optimum. For an arbitrary incidence angle θ_{I}, closed-form expressions for an optimal couple such as (4.6) and (4.7) would be too tedious to obtain. However, the asymptotic approximation of $\mathcal{T}_1(\theta_{\text{I}})$ as a function of (θ, γ) can easily be computed numerically.

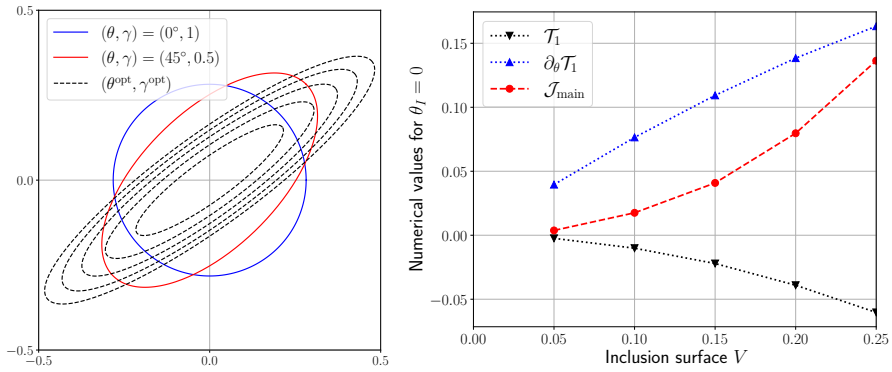

Fig. 8: Left: Investigated ellipses. Test cases with surface $|\Omega_i| = 0.25$ and "optimal" ellipses for normal incidence $\theta_{\rm I} = 0$ with increasing surfaces $|\Omega_i| \in \{0.05, 0.25\}$. Right: Values of $\mathcal{T}_1$, $\partial_\theta\mathcal{T}_1$ and $\mathcal{J}_{\rm main}$, computed numerically for these "optimal" ellipses.

Ellipse	$\mathcal{T}_1$	$\partial_\theta\mathcal{T}_1$	$\mathcal{J}_{\rm main} = (\mathcal{T}_1/\partial_\theta\mathcal{T}_1)^2$
$(\theta,\gamma) = (0°, 1)$ (disk)	-0.11	0	$\emptyset$
$(\theta,\gamma) = (45°, 0.5)$	-0.10	8.6×10^-2	1.4
$(\theta^{\rm opt},\gamma^{\rm opt}) \approx (36°, 0.23)$	-0.06	0.16	0.14

Table 2: Case $\theta_{\rm I} = 0$ (normal incidence). Values of functions $\mathcal{T}_1$, $\partial_\theta\mathcal{T}_1$ and $\mathcal{J}_{\rm main}$ for several ellipses with the same surface $|\Omega_i| = 0.25$, see Figure 8. For the disk, one has $\mathcal{B}_2 = 0$ and therefore $\partial_\theta\mathcal{T}_1 = 0$, so that $\mathcal{J}_{\rm main}$ is not defined.

As illustrated in Figures 9 and 10 for $\theta_{\rm I} = 30°$ and $\theta_{\rm I} = 45°$, respectively, the curves (θ,γ) that achieve $\mathcal{T}_1 = o(\varepsilon^2)$ are numerically extracted, the leading-order approximation of $\partial_\theta\mathcal{T}_1(\theta_{\rm I})$ is computed along them, and an optimal couple is determined, similarly to the case $\theta_{\rm I} = 0$.

For an ellipse with these characteristics and surface $|\Omega_i| = 0.25$, the values of $\mathcal{T}_1$, $\partial_\theta\mathcal{T}_1$ and $\mathcal{J}_{\rm main}$ are then computed by numerically solving the cell problems, and compared the two other ellipses represented in Figure 8. Tables 3 and 4 summarize the results. In these two cases, the "asymptotically optimal" ellipse gives much better results than the two other test-cases.

Ellipse	$\mathcal{T}_1$	$\partial_\theta\mathcal{T}_1$	$\mathcal{J}_{\rm main} = (\mathcal{T}_1/\partial_\theta\mathcal{T}_1)^2$
$(\theta,\gamma) = (0°, 1)$ (disk)	-0.11	0.05	4.8
$(\theta,\gamma) = (45°, 0.5)$	-0.054	0.12	0.20
$(\theta^{\rm opt},\gamma^{\rm opt}) \approx (52°, 0.34)$	-0.019	0.17	0.012

Table 3: Case $\theta_{\rm I} = 30°$. Values of functions $\mathcal{T}_1$, $\partial_\theta\mathcal{T}_1$ and $\mathcal{J}_{\rm main}$ for several ellipses with the same surface $|\Omega_i| = 0.25$.

5. Topological optimization of microstructured interfaces. While in the previous section, we used the analytical information given by the topological derivative to analyse the case of a unique elliptic inclusion, the aim in this section is to use

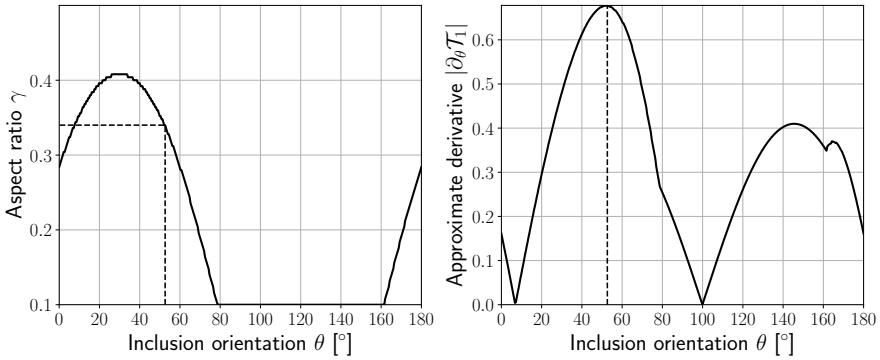

Fig. 9: Case $\theta_{\mathrm{I}} = 30°$. Couples (θ, γ) that achieve $\mathcal{T}_1 = o(\varepsilon^2)$ (left), corresponding leading-order approximation of $\partial_\theta \mathcal{T}_1$ (right), and numerical extraction of the optimal parameters $(\theta^{\mathrm{opt}}, \gamma^{\mathrm{opt}}) \approx (53°, 0.34)$ (dashed lines).

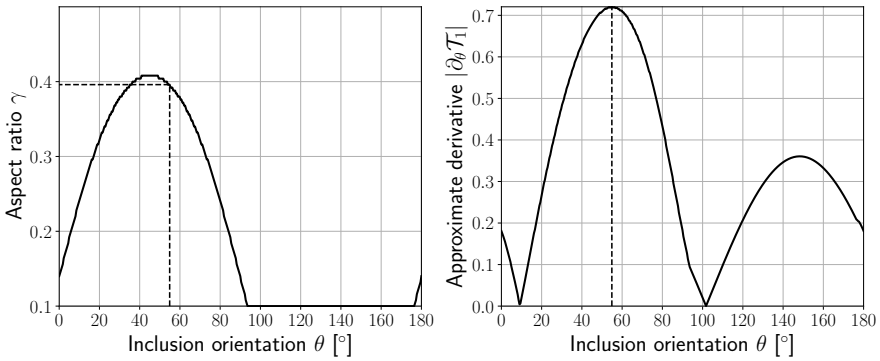

Fig. 10: Case $\theta_{\mathrm{I}} = 45°$. Couples (θ, γ) that achieve $\mathcal{T}_1 = o(\varepsilon^2)$ (left), corresponding leading-order approximation of $\partial_\theta \mathcal{T}_1$ (right), and numerical extraction of the optimal parameters $(\theta^{\mathrm{opt}}, \gamma^{\mathrm{opt}}) \approx (55°, 0.40)$ (dashed lines).

Ellipse	$\mathcal{T}_1$	$\partial_\theta \mathcal{T}_1$	$\mathcal{J}_{\mathrm{main}} = (\mathcal{T}_1/\partial_\theta \mathcal{T}_1)^2$
$(\theta, \gamma) = (0°, 1)$ (disk)	-0.10	0.078	1.8
$(\theta, \gamma) = (45°, 0.5)$	-0.032	0.13	0.058
$(\theta^{\mathrm{opt}}, \gamma^{\mathrm{opt}}) \approx (54°, 0.4)$	-0.011	0.16	0.0047

Table 4: Case $\theta_{\mathrm{I}} = 45°$. Values of functions $\mathcal{T}_1$, $\partial_\theta \mathcal{T}_1$ and $\mathcal{J}_{\mathrm{main}}$ for several ellipses with the same surface $|\Omega_i| = 0.25$.

the topological derivative in an optimization algorithm to minimize a functional with no *a priori* on the geometry of the inclusion. The efficiency of both methodologies will be investigated through numerical examples in Section 5.3.

One aims at generating a microstructure minimizing an objective cost functional $\mathcal{J}(\boldsymbol{m}_{\mathrm{eff}})$. An optimal microstructrure is defined by the phase distribution $\boldsymbol{m}_{\mathrm{opt}}$ in the bounded cell Ω^a. The cost functional depends on the macroscopic behaviour which

is described by the effective parameters $\boldsymbol{m}_{\text{eff}}$ (2.14) that themselves depend on $\boldsymbol{m}$ based on the homogenized model. We therefore consider the following optimization problem:

$$\text{Find} \qquad \boldsymbol{m}_{\text{opt}} = \arg\min_{\boldsymbol{m}} \tilde{\mathcal{J}}(\boldsymbol{m}) \qquad \text{with} \qquad \tilde{\mathcal{J}}(\boldsymbol{m}) = \mathcal{J}(\boldsymbol{m}_{\text{eff}}). \tag{5.1}$$

In this context, and given the optimization problem (5.1), one looks for the topological derivative $\mathcal{D}\tilde{\mathcal{J}}$. If $\mathcal{J}$ is differentiable with respect to the effective parameters, $\mathcal{D}\tilde{\mathcal{J}}$ is computed thanks to the chain rule:

$$\mathcal{D}\tilde{\mathcal{J}} = \frac{\partial \mathcal{J}}{\partial \mathcal{B}}\mathcal{D}\mathcal{B} + \frac{\partial \mathcal{J}}{\partial \mathcal{B}_2}\mathcal{D}\mathcal{B}_2 + \frac{\partial \mathcal{J}}{\partial \mathcal{S}}\mathcal{D}\mathcal{S} + \frac{\partial \mathcal{J}}{\partial \mathcal{C}_1}\mathcal{D}\mathcal{C}_1 + \frac{\partial \mathcal{J}}{\partial \mathcal{C}}\mathcal{D}\mathcal{C}. \tag{5.2}$$

The final objective is to have at hand an optimization algorithm in order to compute the optimal material distribution in the sense of (5.1).

5.1. Optimization scheme.

5.1.1. FFT-based computation of the cell problems. In order to perform topological optimization, multiple computations of the band problem (2.9) are required. Accurately solving this band problem with a numerical efficiency is therefore crucial. The main difficulty compared to classical cell problems with periodicity conditions on all boundaries that are involved in volume homogenization consists in dealing with the unboundedness in the y_1-direction. This problem has been tackled in [16]. This relies on the reformulation of the problem in a bounded cell, which is recalled in Appendix A. Then the solution of this equivalent bounded problem is decomposed as follows

$$\boldsymbol{\Phi} = \boldsymbol{\Phi}_{\text{per}} + \boldsymbol{\Phi}_{\text{bound}}. \tag{5.3}$$

The two terms of this decomposition are

- The bi-periodic function $\boldsymbol{\Phi}_{\text{per}}$ that satisfies:

$$\boldsymbol{\nabla} \cdot \left(\mu(\boldsymbol{y})\left(\boldsymbol{I}_2 + \boldsymbol{\nabla}\boldsymbol{\Phi}_{\text{bound}} + \boldsymbol{\nabla}\boldsymbol{\Phi}_{\text{per}}\right)\right) = \boldsymbol{0} \text{ in } \Omega^a, \tag{5.4}$$

  together with $\int_{\Omega^a} \boldsymbol{\Phi}_{\text{per}} = 1$ for uniqueness. This is an usual cell problem, which appears in homogenization of bi-periodic media, with a source term that is given by $\boldsymbol{I}_2 + \boldsymbol{\nabla}\boldsymbol{\Phi}_{\text{bound}}$. For a given function $\boldsymbol{\Phi}_{\text{bound}}$, this problem is solved using a FFT-accelerated algorithm [28].
- The boundary corrector $\boldsymbol{\Phi}_{\text{bound}}$ that ensures that the boundary conditions associated to the DtN conditions in (2.9) are satisfied:

$$\left(\partial_{\boldsymbol{n}} - \boldsymbol{\Lambda}\right)\boldsymbol{\Phi}_{\text{bound}}\left(\pm\frac{a}{2h}, \cdot\right) = -\left(\partial_{\boldsymbol{n}} - \boldsymbol{\Lambda}\right)\boldsymbol{\Phi}_{\text{per}}\left(\pm\frac{a}{2h}, \cdot\right). \tag{5.5}$$

  Using Fourier series expansion, an explicit expression of the boundary corrector has been proposed in [16].

The problem is then solved using a fixed-point algorithm iterating on $\boldsymbol{\Phi}^n$ whose behaviour has not been investigated theoretically but which has been observed to converge in practice. The various fields are discretized on a regular $N_1 \times N_2$ grid mapping the inner cell Ω^a and the stopping criterion is the following

$$\frac{||\boldsymbol{\Phi}^{n+1} - \boldsymbol{\Phi}^n||_{L^2(\Omega^a)}}{||\boldsymbol{\Phi}^n||_{L^2(\Omega^a)}} < \delta_{\text{FFT}}, \tag{5.6}$$

where δ_{FFT} is a user-chosen parameter.

5.1.2. Material updating. In the configuration mentioned in Introduction, there are only two phases: Ω_m which is the homogeneous matrix outside the microstructured array, and $\Omega_\mathrm{i} \subset \Omega^a$ which is the inclusion phase. Consequently the only material modification allowed in the optimization process is a phase conversion from $(\rho_\mathrm{i}, \mu_\mathrm{i})$ to $(\rho_\mathrm{m}, \mu_\mathrm{m})$ or conversely. Accordingly, the material perturbation $\boldsymbol{\Delta m}$ in the topological derivatives of Proposition 3.23 is chosen as:

$$\boldsymbol{\Delta m} = (\rho_\mathrm{i} - \rho_\mathrm{m}, \mu_\mathrm{i} - \mu_\mathrm{m}) \text{ in } \Omega_m \quad \text{and} \quad \boldsymbol{\Delta m} = (\rho_\mathrm{m} - \rho_\mathrm{i}, \mu_\mathrm{m} - \mu_\mathrm{i}) \text{ in } \Omega_\mathrm{i}. \tag{5.7}$$

Moreover, the shape of the perturbation $\mathcal{P}$ is a disk so that the expression of the polarization tensor is given by (3.27) with $\gamma = 1$. The use of the boundary corrector approach described above requires that the phase at the boundaries $y_1 = \pm\frac{a}{2h}$ is Ω_m. Consequently, one defines an optimization domain

$$\Omega^{\text{design}} = [-b; b] \times [-1/2; 1/2] \quad \text{with} \quad b < \frac{a}{2h}$$

in which material updates are allowed. Since the material is made of two phases, a common way to characterize it is to use a *level-set* function Ψ that satisfies:

$$\begin{cases} \Psi(\boldsymbol{z}) > 0 \text{ in } \Omega^{\text{design}} \cap \Omega_m \\ \Psi(\boldsymbol{z}) < 0 \text{ in } \Omega^{\text{design}} \cap \Omega_\mathrm{i} \end{cases} \quad \text{and} \quad ||\Psi||_{L^2(\Omega^{\text{design}})} = 1. \tag{5.8}$$

A projection algorithm introduced in [6] for topological optimization can then be used [4, 7, 33, 20]. The main steps are recalled in this subsection.

First, one defines a signed normalized topological derivative $\overline{\mathcal{DJ}}^{(n)}$ at iteration n as:

$$\overline{\mathcal{DJ}}^{(n)}(\boldsymbol{z}) = \begin{cases} \mathcal{DJ}^{(n)}(\boldsymbol{z}) / ||\mathcal{DJ}^{(n)}||_{L^2(\Omega^{\text{design}})} \text{ in } \Omega^{\text{design}} \cap \Omega_m \\ -\mathcal{DJ}^{(n)}(\boldsymbol{z}) / ||\mathcal{DJ}^{(n)}||_{L^2(\Omega^{\text{design}})} \text{ in } \Omega^{\text{design}} \cap \Omega_\mathrm{i}. \end{cases} \tag{5.9}$$

When $\overline{\mathcal{DJ}}^{(n)}$ satisfies the sign condition (5.8), then $\mathcal{DJ}^{(n)}(\boldsymbol{z}) > 0$ is satisfied in the whole optimization domain Ω^{design}. Consequently, in this case, the leading-order approximation of the cost functional $\mathcal{J}$ cannot be decreased anymore by a phase change in Ω^{design}. Therefore, $\overline{\mathcal{DJ}}^{(n)}$ satisfying (5.8), is a sufficient optimal condition that ensures that the material configuration corresponds to a local minimum of $\mathcal{J}$. The iterative updating strategy of [6] for Ψ aims at fulfilling this condition. At each iteration, the new level-set function $\Psi^{(n+1)}$ is computed as:

$$\Psi^{(n+1)}(\boldsymbol{z}) = \frac{1}{\sin(\Theta^{(n)})} \left[\sin((1-\kappa^{(n)})\Theta^{(n)}) \Psi^{(n)}(\boldsymbol{z}) + \sin(\kappa^{(n)}\Theta^{(n)}) \overline{\mathcal{DJ}}^{(n)}(\boldsymbol{z}) \right], \tag{5.10}$$

with the angle $\Theta^{(n)}$ being defined by the projection

$$\Theta^{(n)} = \cos^{-1}\left(\overline{\mathcal{DJ}}^{(n)}, \Psi^{(n)} \right)_{L^2(\Omega^{\text{design}})}. \tag{5.11}$$

The parameter $\kappa^{(n)}$ in (5.10) is chosen so that the cost functional decreases at each iteration. In practice, it is initialized to $\kappa^{(0)} = 1$ and then at each iteration it is determined down to a minimal value $\kappa_{\min}$ within an inner optimization loop that writes as:

1. Initalization to $\kappa^{(n)} = \min(2, \kappa^{(n-1)})$

2. While the cost functional does not decrease
   - set $\kappa^{(n)} = \kappa^{(n)}/2$
   - if $\kappa < \kappa_{\min}$, the level-set algorithm is stopped: the cost functional cannot be decreased by the level-set projection

The stopping criterion of the level-set method associated with the updating (5.10) is set as:

$$|\Theta^{(n)}| < \delta_\Theta \tag{5.12}$$

with δ_Θ a user-chosen tolerance parameter.

Remark 5.1. Different initializations are possible for the level-set function $\Psi^{(0)}$, here we chose to compute it as $f/||f||_{L^2(\Omega^{\text{design}})}$ with f being defined by:

$$f(\boldsymbol{z}) = \begin{cases} \bar{\mu} - \mu(\boldsymbol{z}) \text{ if } \mu_{\text{m}} < \mu_{\text{i}}, \\ \mu(\boldsymbol{z}) - \bar{\mu} \text{ if } \mu_{\text{m}} > \mu_{\text{i}}, \end{cases} \tag{5.13}$$

where $\bar{\mu} = (\mu_{\text{m}} + \mu_{\text{i}})/2$.

5.2. Perimeter and surface constraints. One may want to reach a given phase ratio in the microstructure. Consequently, we denote by $\mathcal{A}$ the target surface of phase Ω_{i} in the unit cell, and we now consider the following cost functional:

$$\mathcal{J}_{\text{main}} + \lambda \left(\frac{|\Omega_i|}{\mathcal{A}} - 1 \right)^2 \tag{5.14}$$

where we added a penalization term to tend to satisfy the surface condition. The parameter λ is a user-chosen parameter which is chosen so that the final configuration is made of a surface $|\Omega_i| \in [\mathcal{A} - \mathcal{A}_{\text{err}}; \mathcal{A} + \mathcal{A}_{\text{err}}]$ with $\mathcal{A}_{\text{err}}$ also chosen by the user. An augmented Lagrangian strategy [29] could be carried out rather than this quadratic term with a "user-controlled" parameter λ, but this is beyond the scope of this paper.

Furthermore, for manufacturing purposes, one aims at getting smooth final configurations that are not necessary obtained if we only minimize the cost functional (5.14). Consequently one wants to minimize the following cost functional

$$\mathcal{J}(\boldsymbol{m}_{\text{eff}}) = \mathcal{J}_{\text{main}} + \lambda \left(\frac{|\Omega_i|}{\mathcal{A}} - 1 \right)^2 + \alpha_{\text{per}} \text{Per}(\Omega_{\text{i}}) \tag{5.15}$$

with $\text{Per}(\Omega_{\text{i}}) = \int_{\partial\Omega_{\text{i}}} \mathrm{d}\sigma$ the perimeter of the inclusions phase in a unit cell. In [5], a regularized perimeter functional Per_ϵ has been introduced to take into account perimeter minimization in topology optimization. This functional has been proved to converge to the exact perimeter as the regularization parameter ϵ tends to 0. In practice, the main idea is to solve sequentially the approximate problems for $n = 1, \dots, N_{\text{per}}$:

$$\min \mathcal{J}_{\epsilon_n} := \mathcal{J}_{\text{main}} + \lambda \left(\frac{|\Omega_i|}{\mathcal{A}} - 1 \right)^2 + \alpha_{\text{per}} \text{Per}_{\epsilon_n}(\Omega_{\text{i}}) \tag{5.16}$$

with $\epsilon_{n+1} = \epsilon_n/2$, while ϵ_0 and N_{per} are user-chosen parameters.

5.3. Numerical examples. In this section, the desired macroscopic effect is to minimize the fields along a given direction $\theta_{\min}$ with (r, θ) the polar coordinates centered at $\boldsymbol{X_S} = (-35, 0)$, where the source (2.17) is located. Following the dicussion of Section 2.2, we then want to have a change of sign for $\mathcal{T}_1$ at $\theta_{\min}$. We consequently minimize the regularized cost functional (5.16). The physical parameters are still the one typical of steel in concrete given by Table 1, while the numerical parameters are given in Table 5. In a first example, we chose $\theta_{\mathrm{I}} = 0$ with a surface $\mathcal{A} = 0.2$.

Table 5: Numerical parameters.

$\kappa_{\min}$	δ_Θ	N_1	N_2	δ_{FFT}	ϵ^0	N_{per}
10^{-3}	10^{-1}	101	101	10^{-3}	1	10

In the cost functional (5.16) the coefficients for the surface penalization λ and the perimeter penalization α_{per} are chosen so that $\mathcal{A}_{\mathrm{err}} = 0.06$. Their values for each test case is given in Table 6. Four different initializations are chosen: an ellipse of semi-axes lengths $(0.15, 0.3)$ and tilted of $-\pi/4$, the same ellipse but tilted of $\pi/4$, a random initialization with the same ratio of both materials, and the "asymptotically optimal ellipse" computed in Section 4. The initial configurations, the final configurations obtained after the optimization process, and the maps of the cumulative energy associated with the effective final configurations are plotted for these four cases in Figure 11. The initial and final values of the cost functional are also given in Tables 6 and 7, respectively. We recover the symmetry of the configuration between the first two cases. We observe that the cost functional is well decreased in every example, so we reach a better configuration by topological optimization than with the optimal ellipse. In addition, it seems that the number of iterations and the value of the cost functional are smaller when we initialize by this asymptotically optimal ellipse, so this can be considered as a valuable initialization to improve the results of the topological optimization process. A second example, for $\theta_{\mathrm{I}} = \pi/4$, $\mathcal{A} = 0.3$ and $\mathcal{A}_{\mathrm{err}} = 0.06$ is described by Table 8, Table 9 and Figure 12. It confirms that the topological optimization algorithm decreases the cost functional. However, for the first two initializations the target angle of $\pi/4$ does not seem to be reached so accurately, as it can be noticed in Figures 12c and 12f. In this case, initializing by the optimal ellipse seems even more relevant since the result obtained in Figure 12i is more satisfying, with a cost functional and a number of iterations which are lower than for the other initializations.

Table 6: Initial values for the different configurations with objective $\theta_{\mathrm{I}} = 0$: surface and perimeter parameters, and values of functionals before optimization.

	λ	α_{per}	$\mathcal{J}$ init.	$\mathcal{J}_{\mathrm{main}}$ init.
ellipse $(0.15, 0.3, -\pi/4)$	0.5	0.2	1.21	$9.72 \cdot 10^{-1}$
ellipse $(0.15, 0.3, \pi/4)$	0.5	0.2	1.21	$9.72 \cdot 10^{-1}$
random	0.5	0.2	$5.23 \cdot 10^{3}$	$5.23 \cdot 10^{3}$
optimal ellipse	0.15	$5 \cdot 10^{-2}$	$1.02 \cdot 10^{-1}$	$3.61 \cdot 10^{-1}$

6. Conclusion. In this work, formulas were derived for the sensitivities of the homogenized model that describes the propagation of low-frequency scalar waves

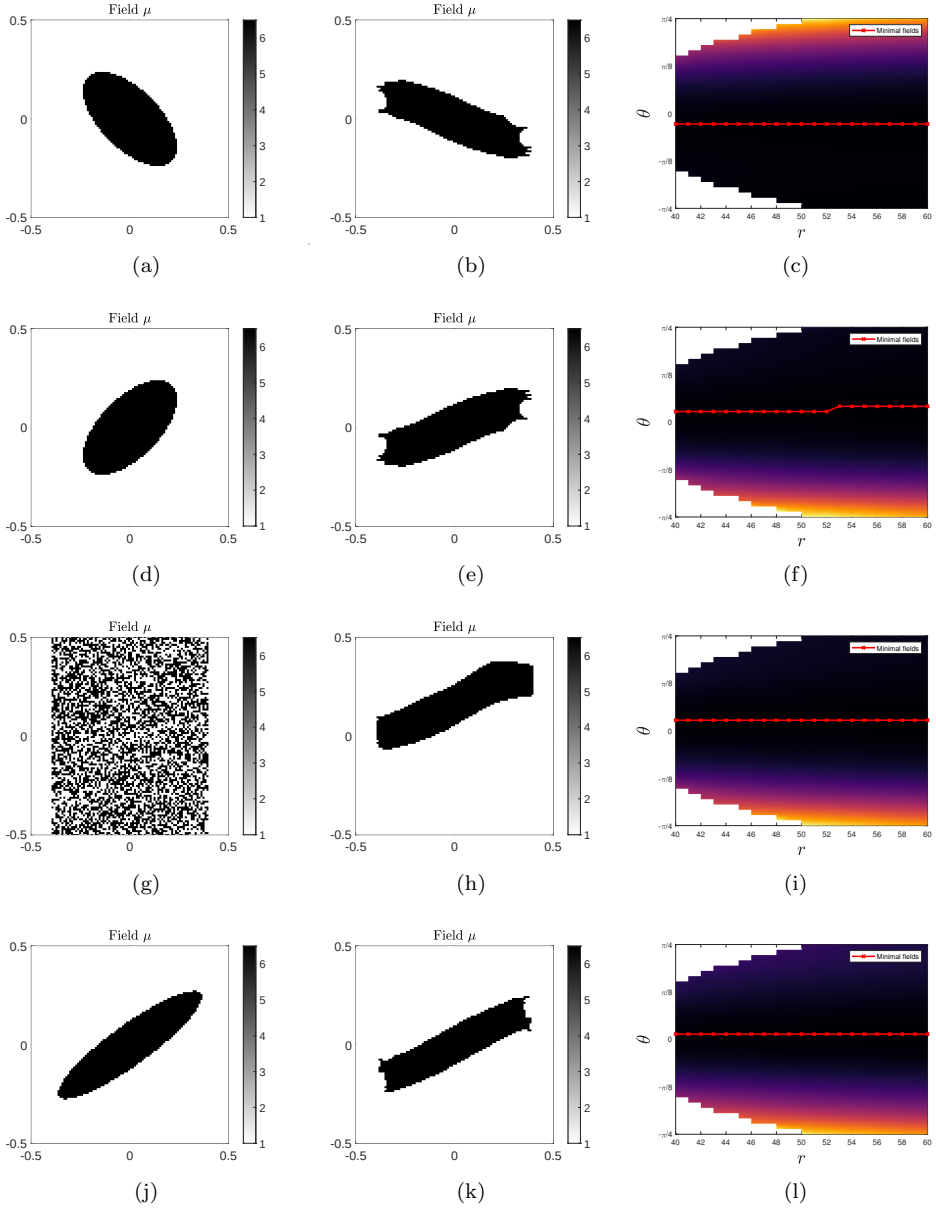

Fig. 11: Test cases for $\theta_{\mathrm{I}} = 0$ and $\mathcal{A} = 0.2$. From left to right: initial configuration, final configuration, and cumulative energy in the effective medium associated to the final configuration where the position of the minimal value for a given r is denoted by the red crosses.

through a row of inclusions embedded in a homogeneous matrix. To do so, we considered asymptotic expansions for a unit cell where a perturbation is introduced. The expression of the sought topological derivatives of the effective parameters involve the solution of band cell problems in an unperturbed unit cell, and the usual polarization

Table 7: Final values for the different configurations with objective $\theta_{\mathrm{I}} = 0$: number of iterations, final surface, and values of functionals after optimization.

	N_{iter}	$\lvert\Omega_i\rvert$ end	$\mathcal{J}$ end	$\mathcal{J}_{\mathrm{main}}$ end
ellipse $(0.15, 0.3, -\pi/4)$	103	0.15	$2.24 \cdot 10^{-1}$	$1.4 \cdot 10^{-2}$
ellipse $(0.15, 0.3, \pi/4)$	103	0.15	$2.24 \cdot 10^{-1}$	$1.4 \cdot 10^{-2}$
random	82	0.16	$1.93 \cdot 10^{-1}$	$7.2 \cdot 10^{-3}$
optimal ellipse	60	0.14	$6.76 \cdot 10^{-2}$	$2.1 \cdot 10^{-3}$

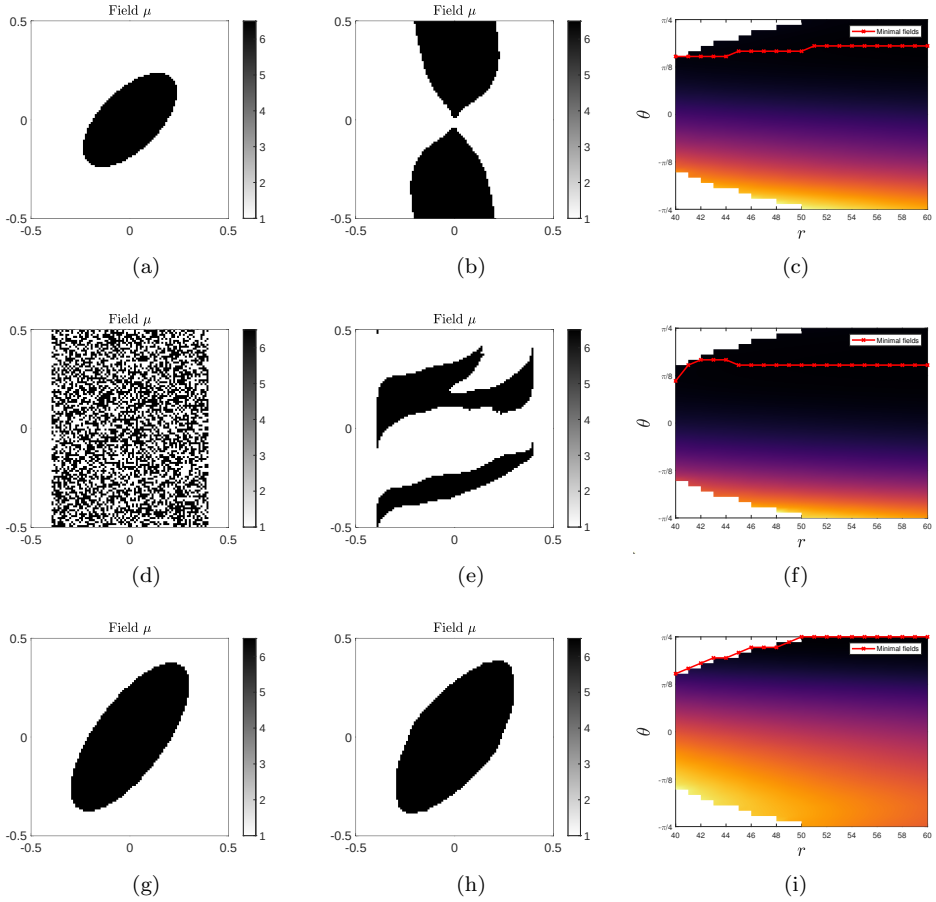

Fig. 12: Test cases for $\theta_{\mathrm{I}} = \pi/4$ and $\mathcal{A} = 0.3$. From left to right: initial configuration, final configuration, and cumulative energy in the effective medium associated to the final configuration where the position of the minimal value for a given r is denoted by the red crosses.

691 tensor. The numerical computation of these band cell problems had been tackled in
692 a previous work, while the polarization tensor is known analytically for elliptic per-
693 turbations, for example. The expression of the topological derivatives were validated

Table 8: Initial values for the different configurations with objective $\theta_{\mathrm{I}} = \pi/4$: surface and perimeter parameters, and values of functionals before optimization.

	λ	α_{per}	$\mathcal{J}$ init.	$\mathcal{J}_{\mathrm{main}}$ init.
ellipse $(0.15, 0.3, \pi/4)$	0.3	$7 \cdot 10^{-2}$	1.51	1.40
random	1	$1 \cdot 10^{-1}$	$2.03 \cdot 10^{-1}$	$2.11 \cdot 10^{-4}$
optimal ellipse	0.3	$7 \cdot 10^{-2}$	$6.27 \cdot 10^{-2}$	$3.30 \cdot 10^{-3}$

Table 9: Final values for the different configurations with objective $\theta_{\mathrm{I}} = \pi/4$: number of iterations, final surface, and values of functionals after optimization.

	N_{iter}	$\lvert\Omega_i\rvert$ end	$\mathcal{J}$ end	$\mathcal{J}_{\mathrm{main}}$ end
ellipse $(0.15, 0.3, \pi/4)$	49	0.30	$2.84 \cdot 10^{-2}$	$9.72 \cdot 10^{-5}$
random	52	0.24	$1.35 \cdot 10^{-1}$	$7.99 \cdot 10^{-4}$
optimal ellipse	28	0.28	$2.96 \cdot 10^{-2}$	$8.76 \cdot 10^{-5}$

numerically, and used to perform an analytical analysis of the sensitivity of the model when considering elliptic inclusions. Then a topological optimization process was developed to minimize a proposed cost functional, which objective was to minimize the transmitted fields along a given direction. The material distribution is updated at each iteration thanks to a level-set method and using the topological derivatives obtained in the first part. Surface and perimeter constraints were also added to the cost functional in order to reach local minima which are smoother and avoid trivial solutions.

This study sets a framework for optimization of microstructured interfaces based on their homogenized properties. This work could be extended to other configurations, for instance:

- resonant interfaces, obtained e.g. for highly contrasted inclusions [39, 38]. In this case, frequency-dependent coefficients have been derived, and while homogenization-based optimization procedures exist for fully periodic resonant media e.g. [40], they are quite scarce for such interfaces, at the best of our knowledge.
- high-frequency behavior. Again, the specific homogenization procedure for higher frequencies or shorter wavelengths is well-known for fully periodic media, and has been used for optimization [32], but could be extended to interfaces.
- *graded* metasurfaces. By relaxing the periodicity assumption and allowing for slow variations of the periodicity cell size along the interface, one may obtain graded interfaces (sometimes called *quasi-periodic* [35]) able to produce stronger macroscopic effects than their strictly periodic counterparts. Optimization procedures also exist for such configuration [30].

Appendix A. Dirichlet-to-Neumann operator.

In this section, the steps used in [16] to obtain the cell problem (2.9) with DtN boundary conditions are briefly recalled. The problem initially derived in [25], posed

in the infinite strip Ω, reads :

$$\text{(A.1)}\qquad \begin{cases} \boldsymbol{\nabla}\cdot\left(\mu(\boldsymbol{y})\left(\boldsymbol{\nabla}_{\boldsymbol{y}}\boldsymbol{\Phi}(\boldsymbol{y})+\boldsymbol{I}_2\right)\right)=\boldsymbol{0} \text{ in } \Omega,\\ \mu(\boldsymbol{y})[\boldsymbol{\nabla}_{\boldsymbol{y}}\boldsymbol{\Phi}(\boldsymbol{y})+\boldsymbol{I}_2]\cdot\boldsymbol{n} \text{ and } \boldsymbol{\Phi} \text{ are continuous on } \partial\Omega_{\mathrm{i}},\\ \boldsymbol{\Phi} \text{ is } y_2\text{-periodic},\\ \lim\limits_{y_1\to\pm\infty}\boldsymbol{\nabla}_{\boldsymbol{y}}\boldsymbol{\Phi}(y_1,y_2)=\boldsymbol{0}. \end{cases}$$

The variations of the physical parameters are restricted to Ω^a due to its definition in (2.7). Introducing the half-strips $\Omega_a^+=[\frac{a}{2h},+\infty[\times I$ and $\Omega_a^-=\,]-\infty,-\frac{a}{2h}]\times I$, see Figure 2, the restrictions $\boldsymbol{\Phi}^{\pm}:=\boldsymbol{\Phi}_{|\Omega_a^{\pm}}$ satisfy $\boldsymbol{\Delta}\boldsymbol{\Phi}^{\pm}=\boldsymbol{0}$ in $\Omega_a^{\pm}$, along with the periodicity and decaying conditions. The modal decomposition of these fields, classically found in the literature on waveguides [22, 13] and also used in [25] to find approximate solutions, then reads:

$$\text{(A.2)}\quad \boldsymbol{\Phi}^{\pm}(y_1,y_2)=\sum_{n\in\mathbb{Z}}\boldsymbol{\varphi}_n^{\pm}\mathrm{e}^{\mp|\xi_n|\left(y_1\mp\frac{a}{2h}\right)}\Psi_n(y_2),\ \text{with}\quad \Psi_n(y_2)=\mathrm{e}^{\mathrm{i}\xi_n y_2},\ \xi_n=2n\pi.$$

The modes $\{\Psi_n\}$ are orthonormal for the L^2 scalar product $(\cdot,\cdot)_I$ on any vertical section I, i.e. they satisfy:

$$\text{(A.3)}\qquad (\Psi_p,\Psi_q)_I=\delta_{pq},\ \text{with}\ (f,g)_I:=\int_I f(y_2)\overline{g(y_2)}\mathrm{d}y_2.$$

Consequently, choosing the particular section $I^+=\left\{(y_1,y_2)\in\Omega_a^+,\,y_1=\frac{a}{2h}\right\}$, see Figure 2, yields the expression of the modal coefficients in the right half-strip:

$$\text{(A.4)}\qquad \boldsymbol{\varphi}_n^+=\left(\boldsymbol{\Phi}^+\left(\frac{a}{2h},\cdot\right),\Psi_n\right)_I=\int_I\boldsymbol{\Phi}^+\left(\frac{a}{2h},y_2\right)\overline{\Psi_n(y_2)}\mathrm{d}y_2.$$

One differentiates the decomposition (A.2) with respect to y_1 and uses the expression of the coefficients (A.4) to get the following *Dirichlet-to-Neumann* (DtN) operator linking the traces of $\boldsymbol{\Phi}$ and of its normal derivative on the section I^+ where $\boldsymbol{\Phi}=\boldsymbol{\Phi}^+$:

$$\text{(A.5)}\quad \partial_{y_1}\boldsymbol{\Phi}\left(\frac{a}{2h},\cdot\right)=\boldsymbol{\Lambda}\left[\boldsymbol{\Phi}\left(\frac{a}{2h},\cdot\right)\right],\ \text{with}\ \boldsymbol{\Lambda}[\boldsymbol{f}](y_2)=-\sum_{n\in\mathbb{Z}}(\boldsymbol{f},\Psi_n)_I\,|\xi_n|\Psi_n(y_2).$$

Similarly, focusing on the particular section $I^-=\left\{(y_1,y_2)\in\Omega_a^-,\,y_1=-\frac{a}{2h}\right\}$, see Figure 2, provides the expression of the "left" modal coefficients of $\boldsymbol{\Phi}^-$. The DtN relation is finally found to be the same for both interfaces $I^{\pm}$, up to the direction of the outer normal derivative:

$$\text{(A.6)}\qquad \partial_{\boldsymbol{n}}\boldsymbol{\Phi}\left(\pm\frac{a}{2h},\cdot\right)=\boldsymbol{\Lambda}\left[\boldsymbol{\Phi}\left(\pm\frac{a}{2h},\cdot\right)\right],\quad \text{where } \partial_{\boldsymbol{n}}=\pm\partial y_1.$$

The problem posed in the infinite band (A.1) can thus be rewritten as the problem (2.9) with DtN boundary conditions on the bounded cell (2.7).

Appendix B. Properties of Green's functions. The definition of the full-space fundamental solution G_∞ in (3.9) implies:

$$\text{(B.1)}\qquad -\mu_\star\Delta_{\boldsymbol{r}}G_\infty(\boldsymbol{r};\mu_\star)=\delta(\boldsymbol{r})\quad\text{and}\quad\boldsymbol{\nabla}_{\boldsymbol{r}}G_\infty(\boldsymbol{r};\mu_\star)=-\frac{\boldsymbol{r}}{2\pi\mu_\star\|\boldsymbol{r}\|^2}.$$

From the problem (3.8), the decomposition of the fundamental solution G given in (3.9) and the equalities above, the complementary part G_c is defined as the solution of the PDE:

$$
\begin{aligned}
-\boldsymbol{\nabla}_{\boldsymbol{y}} \cdot \left(\frac{\mu(\boldsymbol{y})}{\mu_{\mathrm{m}}} \boldsymbol{\nabla}_{\boldsymbol{y}} G_c(\boldsymbol{y}, \boldsymbol{x}) \right) &= \boldsymbol{\nabla}_{\boldsymbol{y}} \cdot \left(\frac{\mu(\boldsymbol{y}) - \mu(\boldsymbol{x})}{\mu_{\mathrm{m}}} \boldsymbol{\nabla}_{\boldsymbol{y}} G_\infty \left(\boldsymbol{y} - \boldsymbol{x}; \frac{\mu(\boldsymbol{x})}{\mu_{\mathrm{m}}} \right) \right) \\
&= -\boldsymbol{\nabla}_{\boldsymbol{y}} \cdot \left(\frac{[\mu(\boldsymbol{y}) - \mu(\boldsymbol{x})] (\boldsymbol{y} - \boldsymbol{x})}{2\pi \mu(\boldsymbol{x}) \|\boldsymbol{y} - \boldsymbol{x}\|^2} \right)
\end{aligned}
\tag{B.2}
$$

along with the boundary conditions:

$$
\begin{cases}
G_c(\cdot, \boldsymbol{x}) + G_\infty \left(\cdot - \boldsymbol{x}; \dfrac{\mu(\boldsymbol{x})}{\mu_{\mathrm{m}}} \right) & \text{is } y_2\text{-periodic,} \\
-\left(\partial_{\boldsymbol{n}} + \Lambda\right) [G(\boldsymbol{y}, \boldsymbol{x})] \Big|_{y_1 = \pm \frac{a}{2h}} = \left(\partial_{\boldsymbol{n}} + \Lambda\right) \left[G_\infty \left(\boldsymbol{y} - \boldsymbol{x}; \dfrac{\mu(\boldsymbol{x})}{\mu_{\mathrm{m}}} \right) \right] \Big|_{y_1 = \pm \frac{a}{2h}} & \forall \boldsymbol{y} \in I^{\pm}.
\end{cases}
\tag{B.3}
$$

The right-hand side of the PDE (B.2) is seen to be regular as $\boldsymbol{y} \to \boldsymbol{x}$ as soon as the material coefficient μ is C^1 in a neighborhood of $\boldsymbol{x}$. Therefore, $G_c(\cdot, \boldsymbol{x})$ and its gradient are ensured to be regular functions when $\boldsymbol{x}$ is itself in the neighborhood of the perturbation point $\boldsymbol{z}$, which is not located on a material interface. Using the rescaled coordinates $(\boldsymbol{y}, \boldsymbol{x}) = (\boldsymbol{z} + \varepsilon \bar{\boldsymbol{y}}, \boldsymbol{z} + \varepsilon \bar{\boldsymbol{x}})$, one obtains the asymptotic behavior:

$$
\boldsymbol{\nabla}_{\boldsymbol{y}} G_c(\boldsymbol{y}, \boldsymbol{x}) = \boldsymbol{\nabla}_{\boldsymbol{y}} G_c(\boldsymbol{z}, \boldsymbol{z}) + o(1) = O(1) \quad \text{as } \varepsilon \to 0. \tag{B.4}
$$

REFERENCES

[1] G. Allaire, F. de Gournay, F. Jouve, and A.-M. Toader, *Structural optimization using topological and shape sensitivity via a level set method*, Control and Cybernetics, 34 (2005), p. 59–80.

[2] G. Allaire and T. Yamada, *Optimization of dispersive coefficients in the homogenization of the wave equation in periodic structures*, Numerische Mathematik, 140 (2018), pp. 265–326, https://doi.org/10.1007/s00211-018-0972-4.

[3] H. Ammari and H. Kang, *Polarization and moment tensors: with applications to inverse problems and effective medium theory*, vol. 162, Springer Science & Business Media, 2007.

[4] S. Amstutz, *Analysis of a level set method for topology optimization*, Optimization Methods and Software, 26 (2011), pp. 555–573, https://doi.org/10.1080/10556788.2010.521557.

[5] S. Amstutz, *Regularized perimeter for topology optimization*, SIAM Journal on Control and Optimization, 51 (2013), pp. 2176–2199, https://doi.org/10.1137/100816997.

[6] S. Amstutz and H. Andrä, *A new algorithm for topology optimization using a level-set method*, Journal of Computational Physics, 216 (2006), pp. 573–588, https://doi.org/10.1016/j.jcp.2005.12.015.

[7] S. Amstutz, S. M. Giusti, A. A. Novotny, and E. A. de Souza Neto, *Topological derivative for multi-scale linear elasticity models applied to the synthesis of microstructures*, International Journal for Numerical Methods in Engineering, 84 (2010), pp. 733–756, https://doi.org/10.1002/nme.2922.

[8] B. Assouar, B. Liang, Y. Wu, Y. Li, J.-C. Cheng, and Y. Jing, *Acoustic metasurfaces*, Nature Reviews Materials, 3 (2018), pp. 460–472, https://doi.org/10.1038/s41578-018-0061-4.

[9] M. P. Bendsøe and O. Sigmund, *Topology Optimization*, Springer Berlin Heidelberg, 2003.

[10] A. Bensoussan, J.-L. Lions, and G. Papanicolaou, *Asymptotic analysis for periodic structures*, AMS Chelsea Publishing, 2011.

[11] M. Bonnet, *Higher-order topological sensitivity for 2-d potential problems. Application to fast identification of inclusions*, International Journal of Solids and Structures, 46 (2009), pp. 2275 – 2292, https://doi.org/10.1016/j.ijsolstr.2009.01.021.

[12] M. Bonnet, R. Cornaggia, and B. B. Guzina, *Microstructural topological sensitivities of the second-order macroscopic model for waves in periodic media*, SIAM Journal on Applied Mathematics, 78 (2018), pp. 2057–2082, https://doi.org/10.1137/17m1149018.

[13] A.-S. Bonnet-Ben Dhia and G. Legendre, *An alternative to Dirichlet-to-Neumann maps for waveguides*, Comptes Rendus Mathematique, 349 (2011), pp. 1005–1009, https://doi.org/10.1016/j.crma.2011.08.006.
[14] D. Cedio-Fengya, S. Moskow, and M. Vogelius, *Identification of conductivity imperfections of small diameter by boundary measurements. continuous dependence and computational reconstruction*, Inverse problems, 14 (1998), p. 553, https://doi.org/10.1088/0266-5611/14/3/011.
[15] R. Cornaggia and C. Bellis, *Tuning effective dynamical properties of periodic media by FFT-accelerated topological optimization*, International Journal for Numerical Methods in Engineering, (2020), https://doi.org/10.1002/nme.6352.
[16] R. Cornaggia, M. Touboul, and C. Bellis, *FFT-based computation of homogenized interface parameters*, Comptes Rendus. Mécanique, 350 (2022), pp. 297–307, https://doi.org/10.5802/crmeca.119.
[17] R. Craster, S. Guenneau, M. Kadic, and M. Wegener, *Mechanical metamaterials*, Reports on Progress in Physics, 86 (2023), p. 094501, https://doi.org/10.1088/1361-6633/ace069.
[18] M. David, C. Pideri, and J.-J. Marigo, *Homogenized interface model describing inhomogeneities located on a surface*, Journal of Elasticity, 109 (2012), p. 153–187, https://doi.org/10.1007/s10659-012-9374-5.
[19] B. Delourme, *Modèles asymptotiques des interfaces fines et périodiques en électromagnétisme*, PhD thesis - Université Pierre et Marie Curie - Paris VI, 2010.
[20] S. Giusti, A. Ferrer, and J. Oliver, *Topological sensitivity analysis in heterogeneous anisotropic elasticity problem. theoretical and computational aspects*, Computer Methods in Applied Mechanics and Engineering, 311 (2016), pp. 134–150, https://doi.org/10.1016/j.cma.2016.08.004.
[21] S. M. Giusti, A. A. Novotny, and E. A. de Souza Neto, *Sensitivity of the macroscopic response of elastic microstructures to the insertion of inclusions*, Proceedings of the Royal Society A: Mathematical, Physical and Engineering Sciences, 466 (2010), pp. 1703–1723, https://doi.org/10.1098/rspa.2009.0499.
[22] I. Harari, I. Patlashenko, and D. Givoli, *Dirichlet-to-Neumann maps for unbounded wave guides*, Journal of Computational Physics, 143 (1998), pp. 200–223, https://doi.org/10.1006/jcph.1998.5960.
[23] B. Lombard, A. Maurel, and J.-J. Marigo, *Numerical modeling of the acoustic wave propagation across an homogenized rigid microstructure in the time domain*, Journal of Computational Physics, 335 (2017), pp. 558–577, https://doi.org/10.1016/j.jcp.2017.01.036.
[24] J.-J. Marigo and A. Maurel, *Homogenization models for thin rigid structured surfaces and films*, The Journal of the Acoustical Society of America, 140 (2016), pp. 260–273, https://doi.org/10.1121/1.4954756.
[25] J.-J. Marigo, A. Maurel, K. Pham, and A. Sbitti, *Effective dynamic properites of a row of elastic inclusions: The case of scalar shear waves*, Journal of Elasticity, 128 (2017), pp. 265–289, https://doi.org/10.1007/s10659-017-9627-4.
[26] J.-J. Marigo and C. Pideri, *The effective behaviour of elastic bodies containing microcracks or microholes localized on a surface*, International Journal of Damage Mechanics, SAGE Publications, 20 (2011), pp. 1151–1177, https://doi.org/10.1177/1056789511406914.
[27] K. Matsushima, H. Isakari, T. Takahashi, and T. Matsumoto, *A topology optimisation of composite elastic metamaterial slabs based on the manipulation of far-field behaviours*, Structural and Multidisciplinary Optimization, 63 (2020), pp. 231–243, https://doi.org/10.1007/s00158-020-02689-y.
[28] H. Moulinec and P. Suquet, *A numerical method for computing the overall response of nonlinear composites with complex microstructure*, Computer Methods in Applied Mechanics and Engineering, 157 (1998), pp. 69–94, https://doi.org/10.1016/s0045-7825(97)00218-1.
[29] J. Nocedal and S. Wright, *Numerical Optimization (Springer Series in Operations Research and Financial Engineering)*, Springer, 2006.
[30] Y. Noguchi and T. Yamada, *Level set-based topology optimization for graded acoustic metasurfaces using two-scale homogenization*, Finite Elements in Analysis and Design, 196 (2021), p. 103606, https://doi.org/10.1016/j.finel.2021.103606.
[31] Y. Noguchi and T. Yamada, *Topology optimization of acoustic metasurfaces by using a two-scale homogenization method*, Applied Mathematical Modelling, 98 (2021), pp. 465–497, https://doi.org/10.1016/j.apm.2021.05.005.
[32] Y. Noguchi, T. Yamada, K. Izui, and S. Nishiwaki, *Topology optimization for hyperbolic acoustic metamaterials using a high-frequency homogenization method*, Computer Methods in Applied Mechanics and Engineering, 335 (2018), pp. 419–471, https://doi.org/10.1016/j.cma.2018.02.031.

[33] J. Oliver, A. Ferrer, J. C. Cante, S. M. Giusti, and O. Lloberas-Valls, *On multi-scale computational design of structural materials using the topological derivative*, in Computational Methods in Applied Sciences, Springer International Publishing, sep 2017, pp. 289–308, https://doi.org/10.1007/978-3-319-60885-3_14.

[34] W. J. Parnell, *The Eshelby, Hill, moment and concentration tensors for ellipsoidal inhomogeneities in the Newtonian potential problem and linear elastostatics*, Journal of Elasticity, (2016), pp. 1–64, https://doi.org/10.1007/s10659-016-9573-6.

[35] K. Pham, N. Lebbe, and A. Maurel, *Diffraction grating with varying slit width: Quasi-periodic homogenization and its numerical implementation*, Journal of Computational Physics, 473 (2023), p. 111727, https://doi.org/10.1016/j.jcp.2022.111727.

[36] K. Pham, A. Maurel, and J.-J. Marigo, *Two scale homogenization of a row of locally resonant inclusions - the case of shear waves*, Journal of the Mechanics and Physics of Solids, 106 (2017), pp. 80–94, https://doi.org/10.1016/j.jmps.2017.05.001.

[37] J. Sanchez-Hubert and E. Sanchez-Palencia, *Introduction aux méthodes asymptotiques et à l'homogénéisation*, Collection Mathématiques Appliquées pour la Maîtrise, 1992.

[38] M. Touboul, B. Lombard, and C. Bellis, *Time-domain simulation of wave propagation across resonant meta-interfaces*, Journal of Computational Physics, 414 (2020), p. 109474, https://doi.org/10.1016/j.jcp.2020.109474.

[39] M. Touboul, K. Pham, A. Maurel, J.-J. Marigo, B. Lombard, and C. Bellis, *Effective resonant model and simulations in the time-domain of wave scattering from a periodic row of highly-contrasted inclusions*, Journal of Elasticity, 142 (2020), pp. 53–82, https://doi.org/10.1007/s10659-020-09789-2.

[40] J. Vondřejc, E. Rohan, and J. Heczko, *Shape optimization of phononic band gap structures using the homogenization approach*, International Journal of Solids and Structures, 113-114 (2017), pp. 147–168, https://doi.org/10.1016/j.ijsolstr.2017.01.038.